Bioactive Materials 6 (2021) 4430–4446

Contents lists available at ScienceDirect

Bioactive Materials

journal homepage: www.sciencedirect.com/journal/bioactive-materials

Zn-Mg and Zn-Cu alloys for stenting applications: From nanoscale mechanical characterization to *in vitro* degradation and biocompatibility

Claudia García-Mintegui [a,b,c], Laura Catalina Córdoba [a,d], Judit Buxadera-Palomero [a,c], Andrea Marquina [a], Emilio Jiménez-Piqué [c,e], Maria-Pau Ginebra [a,c,d], José Luis Cortina [b,c], Marta Pegueroles [a,c,*]

[a] *Biomaterials, Biomechanics and Tissue Engineering Group, Department of Materials Science and Engineering, Technical University of Catalonia (UPC), Barcelona East School of Engineering (EEBE), 08019, Barcelona, Spain*
[b] *Resource Recovery and Environmental Management Group, UPC, EEBE, 08019, Barcelona, Spain*
[c] *Barcelona Research Center in Multiscale Science and Engineering, UPC, EEBE, 08019, Barcelona, Spain*
[d] *Institute for Bioengineering of Catalonia (IBEC), 08028, Barcelona, Spain*
[e] *Structural Integrity, Micromechanics and Reliability of Materials Group, Department of Materials Science and Engineering, UPC, EEBE, 08019, Barcelona, Spain*

ARTICLE INFO

Keywords:
Zinc alloys
Bioresorbable metals
Galvanic corrosion
Nanoindentation
Biocompatibility

ABSTRACT

In the recent decades, zinc (Zn) and its alloys have been drawing attention as promising candidates for bioresorbable cardiovascular stents due to its degradation rate more suitable than magnesium (Mg) and iron (Fe) alloys. However, its mechanical properties need to be improved in order to meet the criteria for vascular stents. This work investigates the mechanical properties, biodegradability and biocompatibility of Zn-Mg and Zn-Cu alloys in order to determine a proper alloy composition for optimal stent performance. Nanoindentation measurements are performed to characterize the mechanical properties at the nanoscale as a function of the Zn microstructure variations induced by alloying. The biodegradation mechanisms are discussed and correlated to microstructure, mechanical performance and bacterial/cell response. Addition of Mg or Cu alloying elements refined the microstructure of Zn and enhanced yield strength (YS) and ultimate tensile strength (UTS) proportional to the volume fraction of secondary phases. Zn-1Mg showed the higher YS and UTS and better performance in terms of degradation stability in Hanks' solution. Zn-Cu alloys presented an antibacterial effect for *S. aureus* controlled by diffusion mechanisms and by contact. Biocompatibility was dependent on the degradation rate and the nature of the corrosion products.

1. Introduction

Coronary artery disease (CAD) is the leading cause of death worldwide and it is characterized by the progressive occlusion of the artery blood flow due to the formation of a plaque. Percutaneous Coronary Intervention (PCI) with stent placement has become the most popular treatment for atherosclerosis, with around three million stents being implanted worldwide each year [1]. The purpose of the cardiovascular stents implantation is to provide support to the artery to avoid vessel recoil during the remodeling process. Although the use of stents has represented a revolutionary advance in the treatment of cardiovascular disease, in-stent restenosis (ISR) and late-stent thrombosis (LST) remain the major limitations of coronary intervention. Bare metal stents (BMS) deployment inside an artery disrupt the healthy endothelium and causes uncontrolled proliferation of smooth muscle cells (SMCs) leading to ISR in 15–30% of PCI. The occurrence of ISR has been reduced to <5% since the introduction of the drug-eluting stents (DES) into clinical routine. However the risk of LST increases due to a delay of endothelial cells (ECs) migration and proliferation and a longer exposition of the plain metal to the blood flow [2]. Thus, a new generation of bioresorbable

Peer review under responsibility of KeAi Communications Co., Ltd.
* Corresponding author. Technical University of Catalonia (UPC), EEBE, Department of Materials Science and Engineering, Av. Eduard Maristany, 10-14, 08019, Barcelona, Spain.
E-mail addresses: claudia.garcia.mintegui@upc.edu (C. García-Mintegui), lcatalina@ibecbarcelona.eu (L.C. Córdoba), judit.buxadera@upc.edu (J. Buxadera-Palomero), andreamarquina95@gmail.com (A. Marquina), emilio.jimenez@upc.edu (E. Jiménez-Piqué), maria.pau.ginebra@upc.edu (M.-P. Ginebra), jose.luis.cortina@upc.edu (J.L. Cortina), marta.pegueroles@upc.edu (M. Pegueroles).

https://doi.org/10.1016/j.bioactmat.2021.04.015
Received 25 October 2020; Received in revised form 9 April 2021; Accepted 13 April 2021
Available online 4 May 2021

stents (BRS) has emerged to overcome the side effects by assisting the arterial healing and dissolving with no implant residues [3].

During the last two decades, bioresorbable materials have been widely investigated for their use in both cardiovascular and orthopedic applications [4–6]. The degradability and resorbability of the materials within the body after implantation simplifies many surgical interventions. The mechanical properties of an ideal stent should be close to those of stainless steel 316L and its total degradation should be fulfilled after one year of the implantation [7]. Bioresorbable polymers predominantly undergo hydrolytic or enzymatic degradation, releasing biocompatible products [8]. Nevertheless, their limited mechanical strength requires thicker struts to match the structural strength of current metallic stents, disrupting laminar blood flow, and potentially increasing the incidence of acute thrombotic events [4]. Magnesium (Mg)- and iron (Fe)-based bioresorbable metals have received much attention in the past years due to their inherent mechanical properties, which make them more attractive stent material candidates than their polymeric counterparts [3,9]. Unfortunately, Mg shows a relatively high degradation rate and release of hydrogen gas which can induce cytotoxicity and can create gas bubbles at the adjacent areas to the implant promoting the separation of the surrounding tissue [10,11]. Fe corrodes at a slow degradation rate for stenting applications and accumulates corrosion products at the artery wall [5,12].

In 2011, zinc (Zn) was proposed as a potential bioresorbable metals for BRS applications with reasonable biocompatibility and an appropriate biodegradation rate between Fe and Mg [13]. However, the development and characterization of Zn and its alloys as bioresorbable metals is an ongoing research and rigorous studies must be performed in order to determine and control their biocompatibility, degradation rate, and optimal mechanical properties. In fact, the risks associated with BRS restrain the growth of the market. Problems are related to limited mechanical material characteristics or unsuitable corrosion characteristics [14]. Nowadays, only Magmaris RMS stent (BIOTRONIK, Germany) bioresorbable metal stent has been CE approved for its clinical use [15]. Thus, a thoroughly understanding of the mechanical properties at the nanoscale of the different alloys phases and the oxidation by-products and species with the biological fluids is needed.

Biocompatibility of Zn alloys and its corrosion products is crucial for stenting applications. Bowen et al. [16] revealed no necrosis or rejection Zn wires when implanted in the abdominal aorta of Sprague-Dawley rats during six months. However, Sherier et al. [17] suggested that free Zn^{2+} ions might hinder cell mobility and adhesion. Kubasek et al. [18] reported a maximum safe Zn^{2+} ion concentration for U2OS and L929 cell lines. Differences in the *in vitro* response depend on the studied alloy, selected cell line and cell culture medium, and the obtained products of corrosion. Zn alloys bacterial response is of interest since stent infection is a rare complication with high mortality (32%), in which the *S. Aureus* and the *P. Aeruginosa* bacteria are responsible for over 80% of the cases [19].

The mechanical properties of Zn are not optimal and thus, different strategies (e.g. alloying, thermal treatments and plastic deformation) have been evaluated. Katarivas Levy et al. [20] reviewed a numerous list of Zn-based formulations along with the reported mechanical properties and corrosion rates, and suggested essential elements Mg, calcium (Ca), copper (Cu), manganese (Mn), and strontium (Sr) as alloying elements for biomedical zinc alloys. Indeed, ternary alloys as Zn-Mg-Ca [21] or Zn-Mg-Cu [22,23] have been evaluated as promising compositions for biodegradable implants. Yang *et al.* [24] performed an extensive evaluation of binary Zn alloys for bioresorbable bone implants. Among all tested conditions, Zn-Li and Zn-Mg alloys showed noteworthy improvements in terms of strength, uniform degradation behavior, and biocompatibility [25,26].

However, the ductility significantly declined with respect to pure Zn, while Zn-Cu alloys have elongation values above 30%, which successfully accomplishes the criteria for cardiovascular stents applications [27]. Moreover, Cu is well-known for its antibacterial properties [1, 28–30] and it is reported to stimulate endothelial cell migration and angiogenesis [31–33]. Alloying with peritectic-forming elements such as Cu or eutectic-forming elements such as Mg, refines the microstructure of pure Zn and enhances its mechanical properties [34,35]. The importance of controlling topography, chemistry, and mechanical properties at micro and nanoscale is fundamental for obtaining the desired cellular response [28]. However, no studies have been devoted to evaluate the mechanical behavior of Zn-Mg and Zn-Cu alloys different phases at the nanoscale depth range.

This work aims to gain a better understanding of the addition of the peritectic and eutectic phases at the Zn matrix and their effect on the corrosion and nanoscale mechanical properties of Zn-Mg and Zn-Cu alloys. To that end, a thoroughly nanoindentation characterization and corrosion evaluation of Zn-based alloys was studied by potentiodynamic polarization (PDP) and electrochemical impedance spectroscopy (EIS) in Hanks' solution. The ion release of the alloys was evaluated through an immersion test by analyzing the released Zn^{2+}, Mg^{2+}, and Cu^{2+} cations. Finally, it has been evaluated the *in vitro* biological response with human aortic endothelial cells (HAoECs), the bacterial activity via agar diffusion tests and the bacterial adhesion with both *S. aureus* and *P. aeruginosa* of Zn-based alloys.

2. Materials and methods

2.1. Materials

Pure Zn (99.9% purity), Zn-xMg (x = 0.5 and 1 wt%) and Zn-xCu (x = 3, and 5 wt%) alloys were provided by Goodfellow, UK, in rods of 10 mm diameter. The as-received condition of Zn was extruded, and Zn-Mg and Zn-Cu bars were extruded and cold rolled. The chemical compositions of the zinc alloys as determined by inductively coupled plasma optical emission spectroscopy (ICP-OES) are presented in Table 1.

2.2. Microstructural characterization

Metallographic samples for the microstructural characterization were prepared from cross-sections and longitudinal samples using standard metallographic procedures followed by etching. The rods were cut into 2.5 mm thick discs, abraded with silicon carbide grinding papers (P800, P1200, P2500 and P4000 from Neuertek S.A., Spain). The grinded samples were polished using 0.05 μm silica suspension (Buehler, Germany) while lubricated with ethanol (≥96% (v/v) Sigma-Aldrich, USA) until achieving smooth surfaces. A previous step of polishing using 6 μm diamond suspension (ATM, Germany) was required for Zn-Cu alloys. All polished samples were ultrasonically cleaned in absolute ethanol (Sigma-Aldrich, USA) and acetone (Sigma-Aldrich, USA) for 5 min. Pure Zn and Zn-Cu alloys were etched by a solution of 200 g/L CrO_3 (Sigma-Aldrich, USA) and 15 g/L Na_2SO_4 (Sigma-Aldrich, USA), and rinsed of 200 g/L CrO_3. Zn-Mg alloys were etched by a solution of 4.2 g picric acid (Sigma-Aldrich, USA), 10 mL acetic acid (Sigma-Aldrich, USA), 70 mL absolute ethanol, and 10 mL of deionized water, and rinsed

Table 1
Chemical composition (wt.%) of Zn-Mg and Zn-Cu alloys determined by ICP-OES.

Sample	Zn (wt. %)	Mg (wt. %)	Cu (wt. %)	Pb (wt. %)	S (wt. %)	Others
Pure Zn	99.939	–	–	0.030	–	<0.02[a]
Zn-0.5Mg	99.393	0.464	–	0.099	–	<0.01[b]
Zn-1Mg	98.498	0.904	–	0.113	–	<0.01[b]
Zn-3Cu	97.144	–	2.708	0.094	0.032	<0.01[c]
Zn-5Cu	95.385	–	4.482	0.084	0.011	<0.01[c]

[a] As, Cd, Sn, Fe.
[b] Ag, Al, As, Cu, S, Se, Si.
[c] Ag, Al, As, Fe, Sb, Se, Si.

in absolute ethanol. Microstructure was observed by scanning electron microscopy (SEM) equipped with X-ray energy-dispersive spectrometry (EDS) (JSM-7001F, JEOL, Japan). X-ray diffractometer (XRD) (D8 ADVANCE Twin, Bruker, USA) using CuKα was operated at 40 kV and 100 mA to identify the phase composition of samples with scanning range from 20° to 90° at a scan rate of 2° min^{-1} and step size of 0.02°. The volume fraction percentage of secondary phase area was calculated using ImageJ software (National Institutes of Health, MD).

2.3. Mechanical characterization

Mechanical properties of the different Zn alloys were evaluated through tensile testing, Vickers micro-hardness, and nanoindentation. The tensile tests were carried out on a universal material test loading machine (Bionix 858 uniaxial, MTS Systems) according to ASTM E8-04 standard [36]. Tensile dog-bone samples (30 mm gage length, 6 mm diameter and 6 mm radius of fillet) were cut from the rolled rods with long axis parallel to the extrusion direction. The tensile tests were carried out at room temperature and at strain rate of 1 mm/min. Fracture surfaces after tensile tests were observed with SEM. Surface micro-hardness, H_v, was measured using a Vickers micro-hardness tester (Durascan G5, Emcotest) with a load of 100 g and dwelling time of 10 s. Mean hardness was averaged from 5 measurements.

Nanoindentations were performed on a MTS Nanoindenter XP equipped with a continuous stiffness measurement (CSM) using a Berkovich diamond tip with its area function determined against fused silica standard. Matrixes of 10 by 10 indentations were done with constant strain rate of 0.05 s^{-1} and a maximum penetration depth of 200 nm. The distance between consecutive indentations was set to 5 μm in order to avoid the interaction of the plastic deformation field between indentations. Results were analyzed with the Oliver and Pharr method [37], usually applied for metallic samples and sharp indenters. This approach minimizes the plastic effects providing a more accurate calculation of the elastic properties of the material [38,39]. Nanoindentation mapping was performed by KLA iMicro nanoindenter (KLA, USA). High-speed nanoindentations performed one complete indentation cycle per second. Matrixes of 60 by 60 indentations were done at constant load up to 2 mN. A constant distance around 5 μm was held between each imprint in order to avoid any overlapping effect. Results were analyzed by InView software (KLA, USA). Prior to nanoindentation studies, the metallic discs were abraded up to 4000 grit and polished with silica.

2.4. Corrosion evaluation

The corrosion behavior of Zn and Zn alloys was studied by potentiodynamic polarization (PDP) test [40], static immersion test [41], and electrochemical impedance spectroscopy (EIS). The solution used for all corrosion tests was Hanks' solution (H4891, Sigma-Aldrich, USA) supplemented with $NaHCO_3$ (Sigma-Aldrich, USA) and $CaCl_2{\cdot}2H_2O$ (Sigma-Aldrich, USA) to simulate the ionic composition of blood plasma but without Mg^{2+} to avoid interfering with the inductively coupled plasma mass spectroscopy (ICP-MS) measurements. The chemical composition of the solution is listed in Table S1. The volume of the solution was 20 mL for all tests. The metallic discs were abraded up to 4000 grit and ultrasonically cleaned with absolute ethanol and acetone. The area of the samples exposed to the solution was 0.79 cm^2 in all cases. For this purpose, Lacomit varnish (Agar Scientific, UK) was used for electrochemically isolate the non-exposed areas.

2.4.1. Potentiodynamic polarization test

Electrochemical analysis was performed in Hanks' modified solution at 37 ± 1 °C and pH 7.4 using a PARSTAT 2273 potentiostat (Princeton Applied Research, USA). Saturated calomel electrode (SCE) and platinum electrode were used as the reference electrode and counter electrode, respectively. After 30 min of stabilization of the open circuit potential (OCP), polarization curves were obtained by scanning from −1.4 to −0.6 V potential against the OCP at a scan rate of 0.16 mV/s, according to ASTM G5-14 [40]. The corrosion current density (i_{corr}) and the corrosion potential (E_{corr}) were determined by extrapolating the cathodic Tafel line with Origin 2020 software (OriginLab, USA). The corrosion rate (CR) (μm/year) was calculated from the corrosion current density using Eq. (1) [42]:

$$CR = 3.27{\cdot}10^{-3}\frac{i_{corr}EW}{\rho} \quad (1)$$

where i_{corr} is the corrosion current density (μA/cm^2), EW is the equivalent metal weight and ρ is the metal density. According to ASTM G102-89 [42], the EW and ρ used for calculation were 32.68, 32.42, 32.15, 33.70, 34.41, and 7.14, 7.11, 7.09, 7.19, 7.23 g/cm^3 for Zn, Zn-0.5Mg, Zn-1Mg, Zn-3Cu, and Zn-5Cu, respectively.

2.4.2. Static immersion test

Static immersion test was performed according to ASTM G31-72 [41]. Samples were first weighted and then totally immersed during 10 days in 20 mL of Hanks' modified solution under non-aerated controlled conditions (T = 37 ± 1 °C, pH 7.4 ± 0.1). The whole solution was renewed every 48 h. Aliquots of the solution collected at 1, 3, 7, and 10 days of immersion time were filtered with 0.2 μm filter and the released concentration of Zn^{2+}, Mg^{2+}, and Cu^{2+} was determined by using ICP-MS (7800 ICP-MS, Agilent Technologies). The redox potential (E) and the pH were monitored during the immersion test with Hanna HI 5521 multiparameter (Hanna Instruments, Italy). After 10 days of immersion, the corrosion products accumulated onto the sample surface were ultrasonically removed with a solution of 200 g/L CrO_3 at 70 °C according to ISO 8407 [43]. Degraded samples were then weighted to calculate the CR through weight loss according to Eq. (2) [41]:

$$CR = (8.76 \cdot 10^4 \times W)/(A \times T \times D) \quad (2)$$

where W is the weight loss (g) after the removal of the corrosion products, A is the sample surface area exposed to the solution (cm^2), T is the immersion time (h), and D is the metal density (g/cm^{-3}).

Surface morphology and chemical composition of the Zn alloys before and after the removal of corrosion products were examined by SEM, EDS, and confocal Raman microscopy (inVia™ Qontor® confocal Raman microscope, Renishaw Inc.).

2.4.3. Electrochemical impedance spectroscopy (EIS)

EIS experiments were carried out in Hanks' solution at 37 ± 1 °C and pH 7.4 ± 0.1 for 7 days. A conventional three-electrode electrochemical cell as described in 2.4.1 was used with an exposed area of the working electrode of 0.8 cm^2. The EIS data were recorded at OCP applying AC amplitude of 10 μA·rms from 10^5 Hz down to 10^{-2} Hz. ZSimpWin v3.21 software, Princeton Applied Research was used to treat the raw data.

2.5. Wettability

Static contact angles (SCA) measurements on Zn and Zn alloys surfaces were performed using a Contact Angle System OCA15 plus (Dataphysics, Germany) with the sessile drop method. All measurements were done at room temperature with 3 μL ultrapure Milli-Q water drop. SCA were calculated at 5, 10, 15, 20, 25, and 30 s after drop deposition using a Laplace-Young fitting with SCA20 software (Dataphysics, Germany). Prior to wettability measurements, the metallic discs were abraded up to 4000 grit and ultrasonically cleaned with absolute ethanol and acetone.

2.6. Antibacterial activity

Staphylococcus aureus (*S. aureus,* CCUG 15915, Culture Collection University of Göteborg (CCUG), Göteborg, Sweden) and *Pseudomonas*

aeruginosa (*P. aeruginosa,* CECT 110, Colección Española de Cultivos Tipo (CECT), Valencia, Spain) were used as Gram positive and Gram negative bacteria model to determine the antibacterial properties of Zn and the Zn alloys samples *in vitro*. Bacteria in frozen stock were aerobically cultured in a brain heart infusion (BHI, Scharlab, Spain) medium at 37 ± 1 °C overnight. Afterwards bacteria were diluted in BHI medium to achieve a final optical density of 0.2 at 600 nm, corresponding to 10^8 colony forming units (CFU) per milliliter.

The inhibition effect on *S. aureus* and P. Aeruginosa of Zn and Zn alloys was measured by the agar diffusion plate test. Agar plates were prepared by mixing the culture medium with 7.5g of agar (Agar bacteriological, Scharlab, Spain). Sterilized agar plates were inoculated with 100 μL of the bacteria suspension at 10^8 CFU/mL. Based on CLSI M07-A9 [44], the samples were sterilized by immersion in ethanol 96% (v/v) for 30 min, washed with phosphate buffered saline (PBS, Sigma-Aldrich) , put in contact with the plates with spread bacteria and incubated at 37 ± 1 °C for 24 h. The antibacterial activity is related to the size of inhibition zone (H), which can be calculated as describes Eq. (3) [44]:

$$H = (D - d)/2 \quad (3)$$

Where H is the inhibition zone in mm, D is the total diameter of specimen and inhibition zone in mm, d is the diameter of specimen in mm. The ideal antibacterial effect occurs when $H \geq 1$. When $H = 0$ and few bacteria are observed, the antibacterial effect is limited; when $H = 0$ and many bacteria observed, there is no antibacterial effect. The image analysis was performed using ImageJ software (National Institutes of Health, MD).

Moreover, the adhesion test was performed by adding 20 μL of the bacteria suspension at 10^8 CFU/mL to each sample and incubating at 37 ± 1 °C for 2h. After incubation, samples were rinsed in PBS three times to remove the non-adhered bacteria. The adhered bacteria were fixed with 500 μL of 2.5% glutaraldehyde in PBS at 5 ± 1 °C for 30 min. Samples were then dehydrated sequentially in a series of ethanol water mixtures (50%, 70%, 90%, 96%, and 100%) for 10 min each. The morphology and number of the adhered bacteria were analyzed by SEM.

2.7. Endothelial cell in vitro assays

Human aortic endothelial cells (HAoEC, 304-05a Cell Applications®) were cultured under standard conditions (humidified atmosphere, 5% CO_2 at 37 ± 1 °C) in Growth Medium ready to use (211–500, Cell applications®) in Nunc tissue culture flasks (Termo Fisher Scientific) and passaged when reached 60–70% confluency. Cell isolation from culture flasks was made by 1 mL-trypsinization (Trypsin/EDTA, Sigma-Aldrich) at room temperature for 5 min followed by cell rinsing and resuspension in Growth Medium. Cells were used for experiments at passage 8–12. Cell viability was determined using cytotoxicity detection kit^{PLUS} lactate dehydrogenase (LDH, Roche®) assay, a microplate reader and calculated as a ratio to the positive control group. Each material was assessed by triplicate.

Cytotoxicity assays were performed according to ISO 10993-5/12 [45,46]. Indirect cell viability of HAoEC was measured after 24 h incubation in supernatant at various dilutions. Prior to cell experiments, the discs were sterilized by immersion for 20 min in ethanol followed by three baths with PBS solution. The supernatants were prepared by immersion of discs (surface finish: polished with 4000 grit emery paper) in Growth Medium ready to use under standard conditions for 3 days at a surface-to-volute ratio of 3 cm^2/mL [46]. Aliquots of supernatants were prepared at 1, 1:1, 1:10, 1:100 and 1:1000 volume-to-volume ratio. Prior to the addition of supernatants, cells were incubated for 24 h in fresh Growth Medium on 96-well plate at a cell density of 10.000 cells/well to allow attachment. After that, the medium was replaced by the diluted supernatants. Cell viability was determined using cytotoxicity detection kit^{PLUS} LDH assay. The optical density was measured at the wavelength of 492 nm using a microplate reader (Synergy HTX, Biotek) and calculated as a ratio to the positive control group.

HAoEC adhesion/proliferation tests were performed for 1 day, 3 days and 7 days (500 μl with 3×10^4 cells/sample). Cells were seeded onto the alloys polished surfaces previously sterilized as described-above and cultured under standard conditions. Experiments were performed by triplicate for viability measurements by LDH assay as described above and additional samples were run for microscopical observation. For this purpose, cells were fixed with 4% paraformaldehyde (PFA, Sigma-Aldrich, USA) for 30 min followed by three baths with PBS solution to remove residual PFA and dehydrated through an ascending series of 50%, 70%, 95% and 100% ethanol for SEM observation. For confocal laser scanning microscopy characterization (Carl ZEISS LSM 800) of viable/dead cells, a double staining Kit (Sigma-Aldrich) of Calcein-AM and Propidium Iodide (PI, Sigma-Aldrich, USA) was used.

2.8. Statistical analysis

The experimental data collected in this study were reported as mean ± standard deviation (SD). Unless previous specified, all physicochemical characterization and cell culture experiments were performed with $n = 3$ samples for each specimen group for each assay used in this study. A normality test (Shapiro-Wilk test) was performed to determine if dataset were modeled by a normal distribution. An equality of variances test (ANOVA) was used to determine statistically significant differences when data were normally distributed. A non-parametric test (Kruskal-Wallis test) was used for non-normally distributed data (p-value < 0.05 for all tests). Statistical analysis was performed using Minitab Statistical Software (Minitab Inc., USA).

3. Results

3.1. Microstructure

Fig. 1 shows SEM images of the microstructure of metallic discs in the cross-section (left) and longitudinal section (right), the detected phases, and their volume fraction. The microstructure of the longitudinal section confirmed the preferential grain orientation due to cold rolling manufacturing for Zn-based alloys (Fig. 1d, f, h, j). Pure Zn microstructure consisted of heterogeneous grains of Zn, ranging from 200 μm up to 1 mm at the cross-section, with partial recrystallization [47]. On the other hand, the microstructure of Zn-Mg alloys consisted of Zn matrix and eutectic mixture of Zn + Mg_2Zn_{11} formed along the grain boundaries of α−Zn (Fig. 1c–f). Image analysis confirmed an increase of the volume fraction for the eutectic mixture from 10% to 19%, for Zn-0.5Mg and Zn-1Mg alloys respectively, with increasing content of alloying element (Fig. S1a-d). Zn-Cu alloys presented a dual-phase microstructure of Zn and the dendritic ε-$CuZn_5$ phase (Fig. 1g–j). Fig. 1h and i showed elongated ε-dendrites and η-Zn grains following the rolling direction. The volume fraction of intermetallic ε-phase significantly increased with the higher percentage of Cu content in the alloy, 7% for Zn-3Cu alloy and 25% for Zn-5Cu alloy (Fig. S1e-f). XRD results confirmed the phases composition of studied samples are in Fig. S2.

3.2. Mechanical properties

Tensile mechanical properties and Vickers hardness results are shown in Fig. 2 with ultimate tensile strength (UTS), yield strength (YS), elongation at break (E%) and Vickers hardness (HV) parameters. Pure Zn showed low values of YS (30 ± 6 MPa), UTS (97 ± 7 MPa), and elongation (8 ± 2%) for this application. As expected, the increasing Mg concentration significantly enhanced the YS up to 192 ± 13 and 222 ± 6 MPa for Zn-0.5Mg and Zn-1Mg, respectively. The UTS values also increased to 219 ± 7 MPa for Zn-0.5Mg, and 260 ± 8 MPa for Zn-1Mg alloy. However, the elongation at break reached 28 ± 6% for Zn-0.5Mg but dramatically decreased down to 11 ± 1% for Zn-1Mg alloy.

The tensile mechanical properties of Zn-Cu alloys were improved

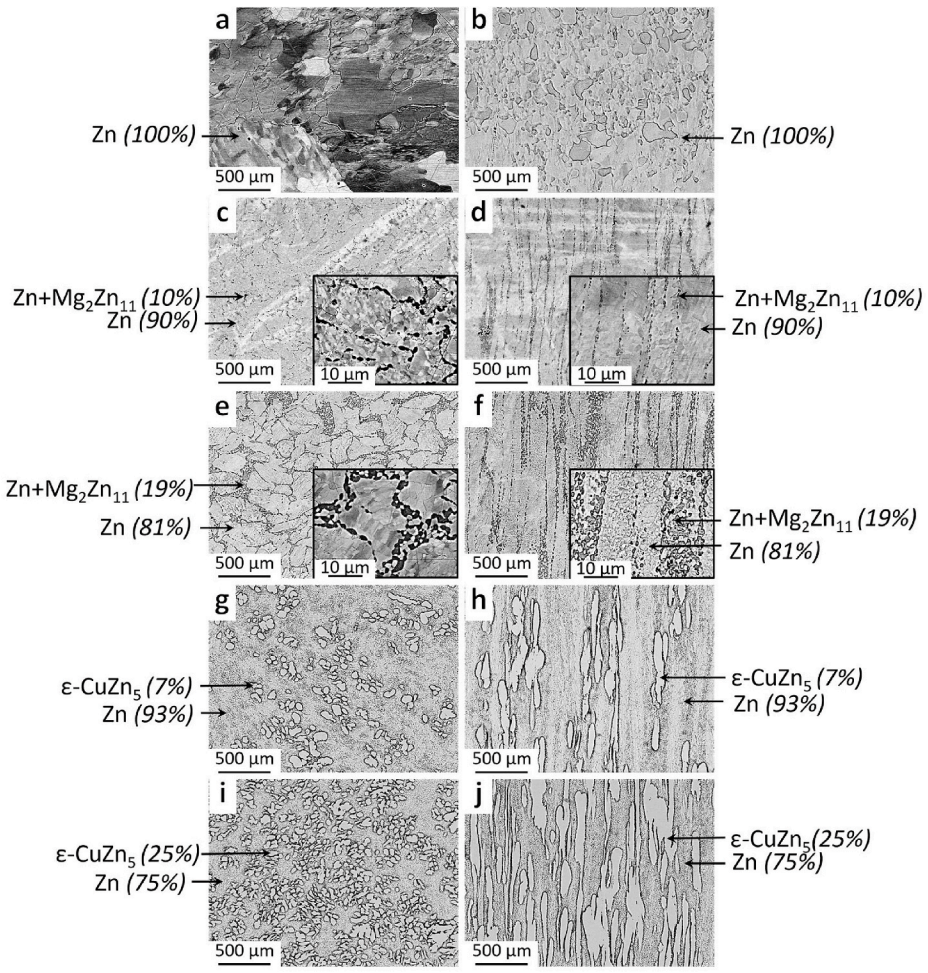

Fig. 1. Microstructure of the cross-section (left) and longitudinal section (right) of: extruded Zn (a, b), and cold rolled Zn-0.5Mg (c, d), Zn-1Mg (e, f), Zn-3Cu (g, h), and Zn-5Cu (i, j) alloys.

compared to pure Zn. Both YS and UTS parameters were 128 ± 4 and 147 ± 1 MPa for Zn-3Cu alloy, and 154 ± 5 and 208 ± 2 MPa, for Zn-5Cu alloy, respectively. As observed, elongation to fracture consistently increased up to 117% for Zn-Cu alloys. No statistical differences in fracture elongation were observed between Zn-3Cu and Zn-5Cu alloys. Vickers micro-hardness of pure Zn resulted of 41 ± 2 HV while Zn-Mg alloys showed higher values up to 90 ± 6 HV for Zn-1Mg alloy (Fig. 2a). This trend is attributed to the increasing volume fraction of the hard Zn + Mg_2Zn_{11} eutectic phase. For Zn-Cu alloys, the hardness was also enhanced up to 73 ± 5 HV for Zn-5Cu alloys, correlated with the larger the volume fraction of ε-$CuZn_5$ intermetallic phase.

The morphology of the fracture surfaces after tensile testing tests is shown in Fig. 2b. The fracture surface of pure Zn presented fully *trans*-granular morphology, indicating a brittle fracture without plastic deformation, in accordance to its low fracture elongation (8 ± 2%). Zn-0.5Mg alloy exhibited dimple-fracture features, which is consistent with the enhanced elongation to fracture (28 ± 6%) compared to pure Zn. The number of plastic dimples decreased with the increasing in Zn-1Mg alloy, and the predominance of cleavage planes confirmed the macroscopic fragility and lower elongation to fracture (11 ± 1%). Zn-Cu alloys fracture surface exhibited a ductile fracture behavior, coherent with the larger elongation at break value of around 117%. The magnitude of the ridges suggested more refined microstructure of Zn-Cu alloys when compared to Zn, and larger grain size than Zn-Mg alloys.

As shown in Fig. 3, nanoindentations on Zn matrix and secondary phases (eutectic Zn + Mg_2Zn_{11} for Zn-Mg alloys, and peritectic ε-$CuZn_5$ for Zn-Cu alloys) provided the hardness and elastic modulus (E) of each specific phase (Table 2). The Zn matrix showed hardness of 1.11 ± 0.08 GPa for pure Zn. Statistically higher values for Zn-0.5Mg, and Zn-1Mg alloys (1.18 ± 0.15, and 1.19 ± 0.12 GPa, respectively), and statistically lower values for Zn-3Cu (0.82 ± 0.13 GPa) and Zn-5Cu (0.84 ± 0.15 GPa) were reported. E values ranged from 71 up to 89 GPa but no statistical differences were found between studied surfaces.

High-speed nanoindentation test provided values of Zn matrix hardness of 0.89 ± 0.272, 1.104 ± 0.216, and 1.112 ± 0.329 GPa for pure Zn, Zn-1Mg, and Zn-3Cu, respectively. The reported hardness of the ε-$CuZn_5$ secondary phase was 2.008 ± 0.328 GPa, and higher hardness was obtained for Zn + Mg_2Zn_{11} (2.684 ± 0.457 GPa). Hardness histograms and maps compiled from the high-speed nanoindentation test are shown in Fig. S3. The E values of Zn matrix were 69.73 ± 11.88, 72.47 ± 9.41, and 75.36 ± 17.32 GPa for Zn, Zn-1Mg, and Zn-3Cu, respectively. The E of secondary phases was 95.70 ± 9.15 GPa, for Zn + Mg_2Zn_{11}, and 109.92 ± 11.26 GPa for $CuZn_5$.

3.3. Corrosion behavior

3.3.1. Potentiodynamic polarization test

The corrosion resistance of the alloys was first evaluated by potentiodynamic measurements in modified Hanks' solution at 37 ± 1 °C. Prior, OCP curves measured upon stabilization are presented in Fig. S4. The most representative polarization curves for pure Zn and Zn alloys are shown in Fig. 4. The behavior of the cathodic region was similar for all materials, whereas some differences were observed in the anodic region as a function of the alloy composition. In all cases, a net anodic

a

Sample	YS (MPa)	UTS (MPa)	Elongation at break (%)	Micro-hardness (HV)
Pure Zn	30 ± 6	97 ± 7	8 ± 2	41 ± 2
Zn-0.5Mg	192 ± 13	219 ± 7	28 ± 6	73 ± 2
Zn-1Mg	222 ± 6	260 ± 8	11 ± 1	90 ± 6
Zn-3Cu	128 ± 4	147 ± 1	117 ± 14	67 ± 3
Zn-5Cu	154 ± 5	208 ± 2	117 ± 21	73 ± 5

b

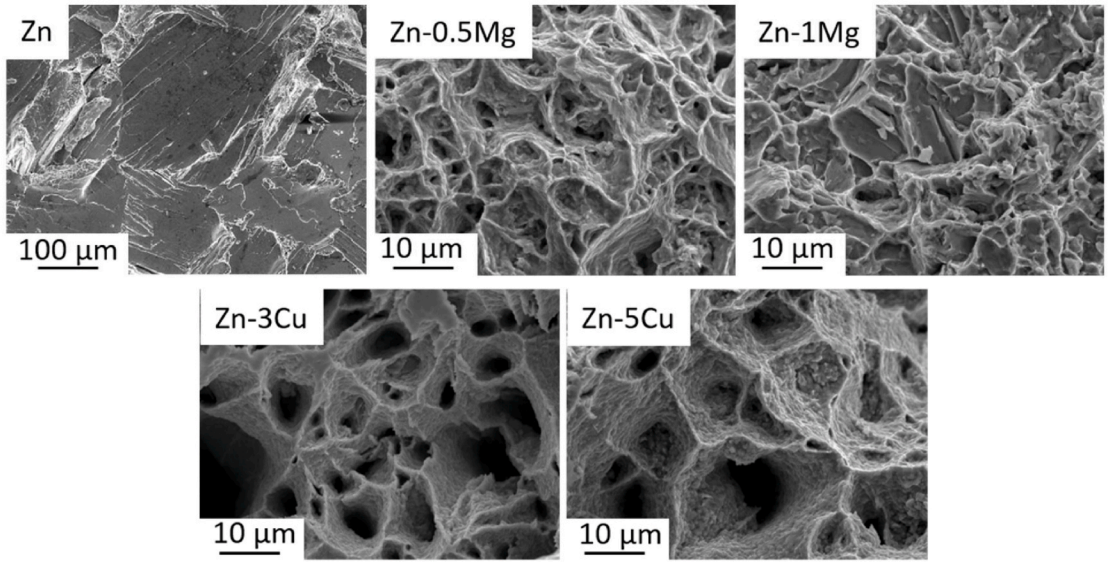

Fig. 2. Tensile test of pure Zn and Zn-Mg and Zn-Cu alloys: a) mechanical parameters obtained after tensile and micro-hardness testing. [a, b,] symbols join groups with non-statistically significant differences. b) SEM morphology of the tensile fracture surfaces.

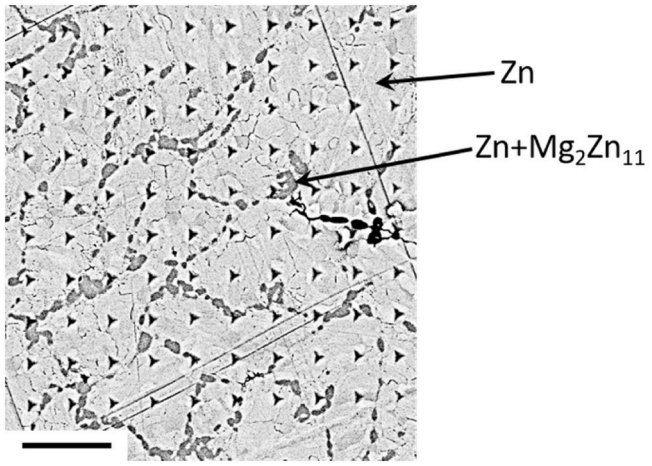

Fig. 3. SEM image of nanoindented Zn-0.5Mg alloy with the matrix of 10 by 10 nanoindentations and the phases composition. Scale bar: 10 µm.

potential was observed at approximately −1.1 V (see E_{corr} in Table 3).

Three regions are observed in the anodic branch: first, an activation region around the E_{corr}; followed by a passive region where potential shifts towards to more positive values with low variation of current density; and finally, a third region where it is detected a change in the anodic-current slope around −0.9 V. In the case of Zn-3Cu and Zn-5Cu, the passive region is not as pronounced as in the case of Zn, Zn-0.5Mg and Zn-1Mg. The passive region for Zn-5Cu is much smaller than that of the other materials, with an evident breakdown of the passive corrosion layer at about −1.0 V. The constant increasing of the current density for Zn-3Cu and Zn-5Cu above E_{corr}, suggest that the passive layer

Table 2
Elastic modulus and hardness of the zinc matrix and the secondary phases of the tested samples.

Surface	Zn matrix		Secondary phase[a]	
	Hardness (GPa)	E (GPa)	Hardness (GPa)	E (GPa)
Pure Zn	1.11 ± 0.08[a]	89 ± 5	n.d.	n.d.
Zn-0.5Mg	1.18 ± 0.15[b]	80 ± 12	2.50 ± 0.64[a]	98 ± 2[a]
Zn-1Mg	1.19 ± 0.12[b]	71 ± 21	2.65 ± 0.46[a]	100 ± 11[a]
Zn-3Cu	0.82 ± 0.13[c]	75 ± 5	1.85 ± 0.33[b]	104 ± 5[b]
Zn-5Cu	0.84 ± 0.15[c]	80 ± 9	1.84 ± 0.43[b]	106 ± 4[b]

[a] Zn + Mg_2Zn_{11} for the Zn-Mg alloys, and ε-$CuZn_5$ for the Zn-Cu alloys, n.d. not determined.[a,b,c] symbols join groups with non-statistically significant differences.

formed on these alloys is less protective than the layer formed on Zn and the Zn-Mg alloys. Moreover, Zn-Mg alloys displayed higher anodic current density than Zn-Cu alloys and pure Zn (see i_{corr} in Table 3). The calculated CR from potentiodynamic curves was around 0.03 mm/year for all samples (see CR from PDP test in Table 3).

3.3.2. Static immersion test

CR was calculated from degraded samples after 10 days of immersion into modified Hank's solution and subsequent removing of corrosion products, obtaining a value of approximately 0.1 mm/year for all samples (see CR, immersion test in Table 3). Fig. 5a shows the curves of Zn^{2+} release after 1, 3, 7, and 10 days of immersion in Hanks' solution. The released Zn^{2+} reached a maximum between 100 and 150 µg/dL at day 1, and decreased towards a minimum below 8.0 µg/dL at day 10 for all samples. For Zn-Mg alloys, the Mg^{2+} concentration detected was below 10 µg/dL. The detection limit for ICP-MS is 0.01 µg/dL, and Cu^{2+} cations were not detected in any case. Indicating that Cu^{2+} concentration in

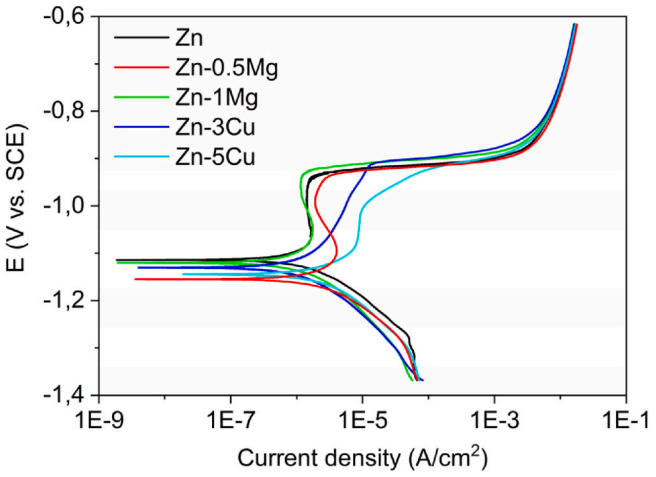

Fig. 4. Potentiodynamic polarization curves of Zn, Zn-0.5Mg, Zn-1Mg, Zn-3Cu, and Zn-5Cu in Hanks' solution at 37 ± 1 °C.

Table 3
Corrosion parameters obtained from PDP test (E_{corr}, i_{corr}, and CR), and calculated CR by weight loss after 10 days of immersion in Hanks' solution at 37 ± 1 °C and pH 7.4.

Surface	Corrosion parameters from PDP test			CR, immersion test (mm/year)
	E_{corr} (V)	i_{corr} (μA·cm^{-2})	CR, PDP test (mm/year)	
Pure Zn	−1.1237 ± 0.0171	2.10 ± 0.05	0.031 ± 0.001	0.132 ± 0.046
Zn-0.5Mg	−1.1289 ± 0.0348	2.34 ± 0.29	0.035 ± 0.004	0.115 ± 0.004
Zn-1Mg	−1.1298 ± 0.0202	2.45 ± 0.65	0.036 ± 0.010	0.105 ± 0.017
Zn-3Cu	−1.1479 ± 0.0215	2.02 ± 0.56	0.031 ± 0.009	0.094 ± 0.005
Zn-5Cu	−1.1293 ± 0.0234	2.21 ± 0.51	0.034 ± 0.008	0.103 ± 0.009

inorganic Hanks' solution was lower than 0.01 μg/dL.

Fig. 5b showed a pH increase from 7.4 ± 0.1 of Hanks' solution during the immersion test confirming the corrosion of all studied samples. Finally, negative values of redox potentials were maintained during the degradation of all samples, maintaining the redox homeostasis for a normal physiological steady state (Fig. 5c) [48]. SEM images of the corroded samples before and after the removal of the corrosion products are presented in Fig. 6. SEM images of corroded surfaces showed similar rounded-features for pure Zn (Fig. 6a) and Zn-5Cu (Fig. 6i). The Zn-0.5Mg alloy combined these rounded-shapes with crystals with morphology typical of hydroxyapatites (Fig. 6c), which formed a uniform corrosion layer in the case of the Zn-1Mg alloy (Fig. 6e). EDS confirmed the presence of Ca, O and P. The corrosion products of Zn-3Cu alloy were clustered in specific areas suggesting localized corrosion (Fig. 6g). EDS analysis confirmed the presence of Zn, Ca, C, O, P, and Cl in the corroded surfaces of the samples. Mg and Cu were detected at the surface of corroded Zn-Mg alloys and Zn-Cu alloys, respectively. Raman spectra of the corroded mineral surfaces (Fig. S5) confirmed the presence of complex Zn mineral phases (*simonkolleite* ($Zn_5(OH)_8Cl_2{\cdot}H_2O$), *hydrozincite* ($Zn_5(CO_3)_2(OH)_6$) and *skorpionite* ($Ca_3Zn_2(PO_4)_2{\cdot}CO_3(OH)_2{\cdot}H_2O$)), and hydroxyapatite (Fig. S5).

After removal of the corrosion products, a uniform corroded surface of pure Zn was revealed (Fig. 6b). On the other hand, micro-galvanic activity between Zn matrix and the secondary phases for the alloys confirmed galvanic corrosion mechanisms. SEM images of the corroded surfaces of Zn-Mg alloys (Fig. 6d, f) indicated faster degradation of Zn + Mg_2Zn_{11} eutectic than Zn matrix over all surfaces. On the contrary, Zn-Cu alloys showed areas nearly impassive and others with localized corrosion in which the degradation of Zn matrix is preferred over the ε-$CuZn_5$ phase (Fig. 6h, j). The powerful galvanic cell Zn/ε-$CuZn_5$ led to noticeable galvanic corrosion in Zn-5Cu alloy (Fig. 6j).

The release of Zn^{2+} reached a maximum after 24 h of immersion and decreased to a minimum after 10 days. At every time point, the total Zn^{2+} concentration in solution is within the range of regular blood zinc level (60–240 μg/dL) [49,50]. Although similar CR values were obtained from weight difference, different corrosion mechanisms were evidenced. Uniform degradation behavior was evidenced for pure Zn. However, the presence of secondary phases forms galvanic pairs with Zn matrix that resulted in galvanic corrosion. The degradation of both Zn + Mg_2Zn_{11} eutectic and ε-$CuZn_5$ peritectic has been observed. Faster degradation of Zn + Mg_2Zn_{11} than Zn matrix was observed all over the surface of Zn-Mg alloys, whereas Zn-Cu alloys showed points of localized corrosion in which the ε-$CuZn_5$ peritectic remained impassive and Zn matrix considerably degraded. This behavior is coherent with the polarization curves that showed less protective passive film for Zn-Cu alloys than those for Zn-Mg alloys (Fig. 4).

3.3.3. Corrosion evolution by EIS

The corrosion behavior of Zn and the four Zn alloys was determined by EIS measurements at OCP. The most representative Nyquist plots of all materials and the equivalent circuits (EC) are depicted in Fig. 7. The corrosion degradation behavior was based on the formation and breakdown of the corrosion products layer as previously reported [51–53].

The Nyquist plots for pure Zn (Fig. 7b) and Zn-0.5Mg alloy (Fig. 7c) evidenced dynamic corrosion mechanisms where initially a corrosion layer was formed, followed by its rupture at later stages. Two capacitive loops appeared for pure Zn at 2 h after immersion. The high frequency capacitive loop could be assigned to charge transfer resistance, and the mid-frequency capacitive loop could be attributed to the electrolyte resistance inside the corrosion film pores. The EC used for the fitting the experimental data is presented in Fig. 7a,ii. The circuit consists of the following elements: R_s (solution resistance), R_{ct} (charge transfer resistance), CPE_{dl} (double layer capacitance), R_f (resistance of the solution inside the pores of the corrosion film), and Warburg component (W) which represents diffusion controlled processes through the corrosion layer [54]. The impedance modulus (|Z|) of pure Zn at 2 h was 3389 Ω cm^2 and decreased down to 2501 Ω cm^2 at 4 h, indicating the progression of the corrosion processes. The evolution of |Z| suggested that the corrosion layer appeared between 4 and 8 h. After 8 h of immersion, the mid-frequency loop transformed and better fitted to an EC without W component (Fig. 7a,i), suggesting a densification of the corrosion film. The local breakdown of this film was recorded after 26 h. The increase of |Z| up to 2018 Ω cm^2 at 2 days could be assigned to the thickening of a corrosion film, whose barrier properties were deteriorated after 7 days of immersion leading to lower corrosion resistance (|Z| = 1516 Ω cm^2).

Fig. 7c shows the Nyquist plots of Zn-0.5Mg alloy. A corrosion layer appeared after 4 h of immersion (fitted to Fig. 7a,i). At 8 h of immersion the Nyquist plots fitted to the EC shown in Fig. 7a,iii, which is modeled by an inner layer (R_{il}, CPE_{il}) and an outer layer (R_{ol}, CPE_{ol}) [51]. Here, the inner layer and the outer layer corresponded to the oxide film initially formed and the later deposited hydroxyapatite crystals shown in Fig. 6c, respectively. The |Z| of Zn-0.5Mg decreased from 2138 Ω cm^2 at 3d to 1213 Ω cm^2 at 7d, suggesting the deterioration of the corrosion layer (fitted to Fig. 7ii).

In the case of Zn-1Mg, the |Z| decreased from 2 h to 8 h (Fig. 7d). After 8 h, the increase of |Z| suggested a corrosion layer formation. Beyond 2 days, minor fluctuations of |Z|, which was 2100 Ω cm^2, were observed; this indicated a more stable corrosion products film compared to those formed on Zn and Zn-0.5Mg. EC used for the fitting was Fig. 7ii.

The impedance of Zn-3Cu (Fig. 7e) continuously decreased from 2 h to 2 days. After this period, |Z| slightly raised and stabilized about 1300 Ω cm^2. In the case of Zn-5Cu (Fig. 7f), it showed a rather stable behavior

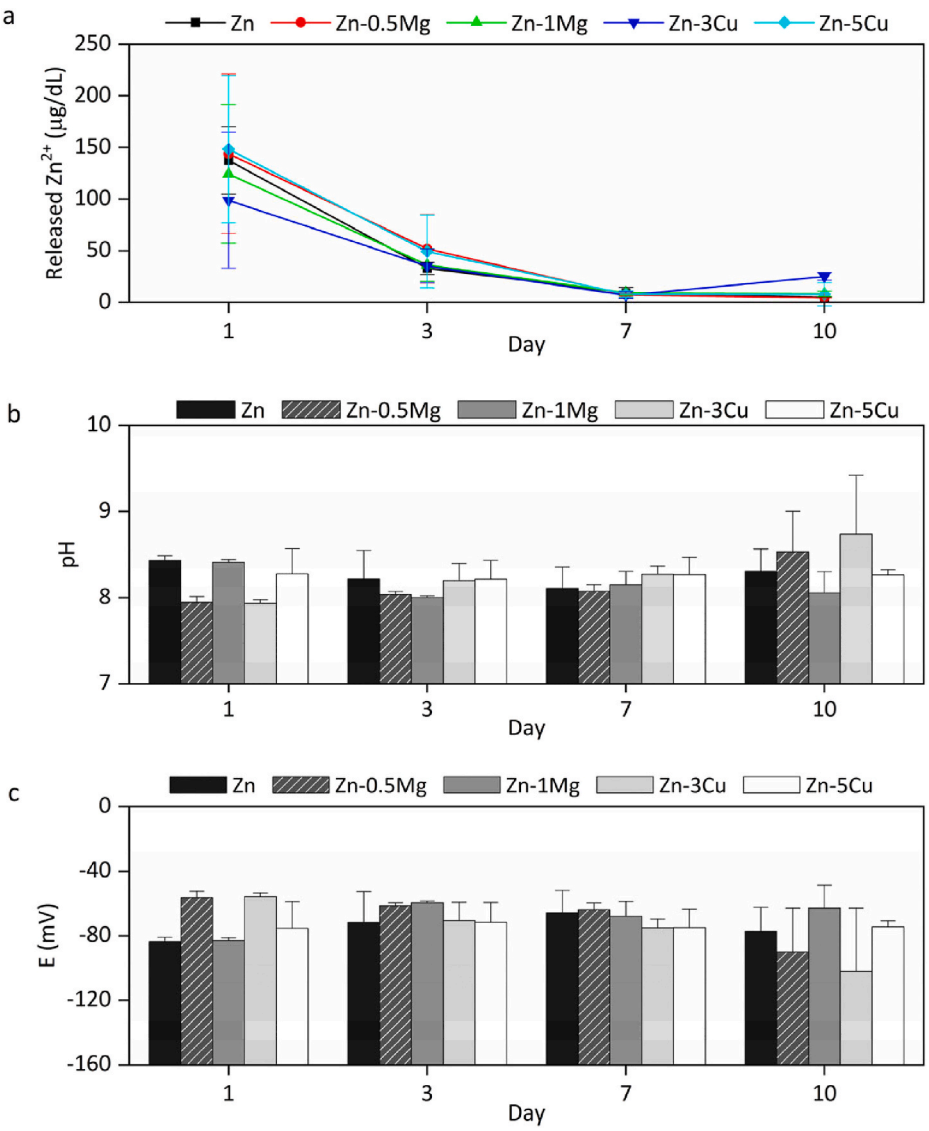

Fig. 5. Immersion evaluation of studied Zn and Zn-based surfaces after 1, 3, 7, and 10 days in Hanks' solution at 37 °C: (a) Values of released Zn^{2+} expressed as (μg/dL), (b) pH, and (c) redox potential.

at early immersion (2 h–8 h) after which |Z| had a sharp drop between 8 and 26 h (both Zn-Cu alloys fitted to Fig. 7a,ii). After 26 h, impedance of Zn-5Cu slightly increased and continued with minor fluctuations over the remaining of the immersion. The curves fitted to the EC in Fig. 7d. In general, both Zn-Cu alloys showed lower corrosion resistance than the Zn-Mg alloys in Hanks' solution under the here studied conditions.

3.4. Wettability

Fig. S6 illustrates the wettability of studied Zn and Zn-based alloys with deionized water. For all studied surfaces, the contact angle slightly decreased with increasing deposition time, but no statistically significant differences were observed after 30 s. The contact angle of pure Zn at 5 s after the deposition of the droplet was 91.70 ± 1.03°. The Zn-Cu alloys were more hydrophobic (92.71 ± 0.70° for Zn-3Cu; and 97.32 ± 3.61° for Zn-5Cu), while the Zn-Mg alloys showed a more hydrophilic behavior compared to Zn (87.19 ± 0.60° for Zn-0.5Mg; and 85.73 ± 1.65° for Zn-1Mg). The wettability behavior of Zn-Mg and Zn-Cu alloys may be attributed to changes in the surface chemistry. Chemically heterogeneous surfaces (as multiphase alloys) count with multiple states individually associated with a local minimum in the Gibbs energy [55]. Here, samples series with higher fraction of Zn + Mg_2Zn_{11} are more hydrophilic, whereas series with higher ε-$CuZn_5$ shown a more hydrophobic behavior.

3.5. Antibacterial activity

Agar diffusion test showed no inhibition zone for *S. Aureus* cultured on pure Zn, Zn-0.5Mg, and Zn-1Mg, indicating no antibacterial effect. On the opposite, both Zn-Cu alloys manifested inhibition zone of 1 mm size (1 ± 0.07 mm for Zn-3Cu, and 0.88 ± 0.03 mm for Zn-5Cu). Moreover, no inhibition zone was observed for *P. Aeruginosa* bacteria for any studied surface.

Fig. 8 shows the SEM images of the morphology of adhered *S. aureus* and *P. aeruginosa* after 2 h of culturing on the investigated samples. No morphology changes were observed in the *S. aureus* after 2 h in contact with the samples. However, the number of adhered bacteria on Zn-Mg alloys increased compared to pure Zn (Fig. 8a, c, e). On the other hand, there was much less *S. aureus* adhesion on the Zn-Cu alloys (Fig. 8g, i), especially the Zn-5Cu alloy, which showed an anti-adhesion performance against the *S. aureus*. Moreover, localized evidences of degradation of the Zn-5Cu surface were observed (Fig. 8i). The adhesion

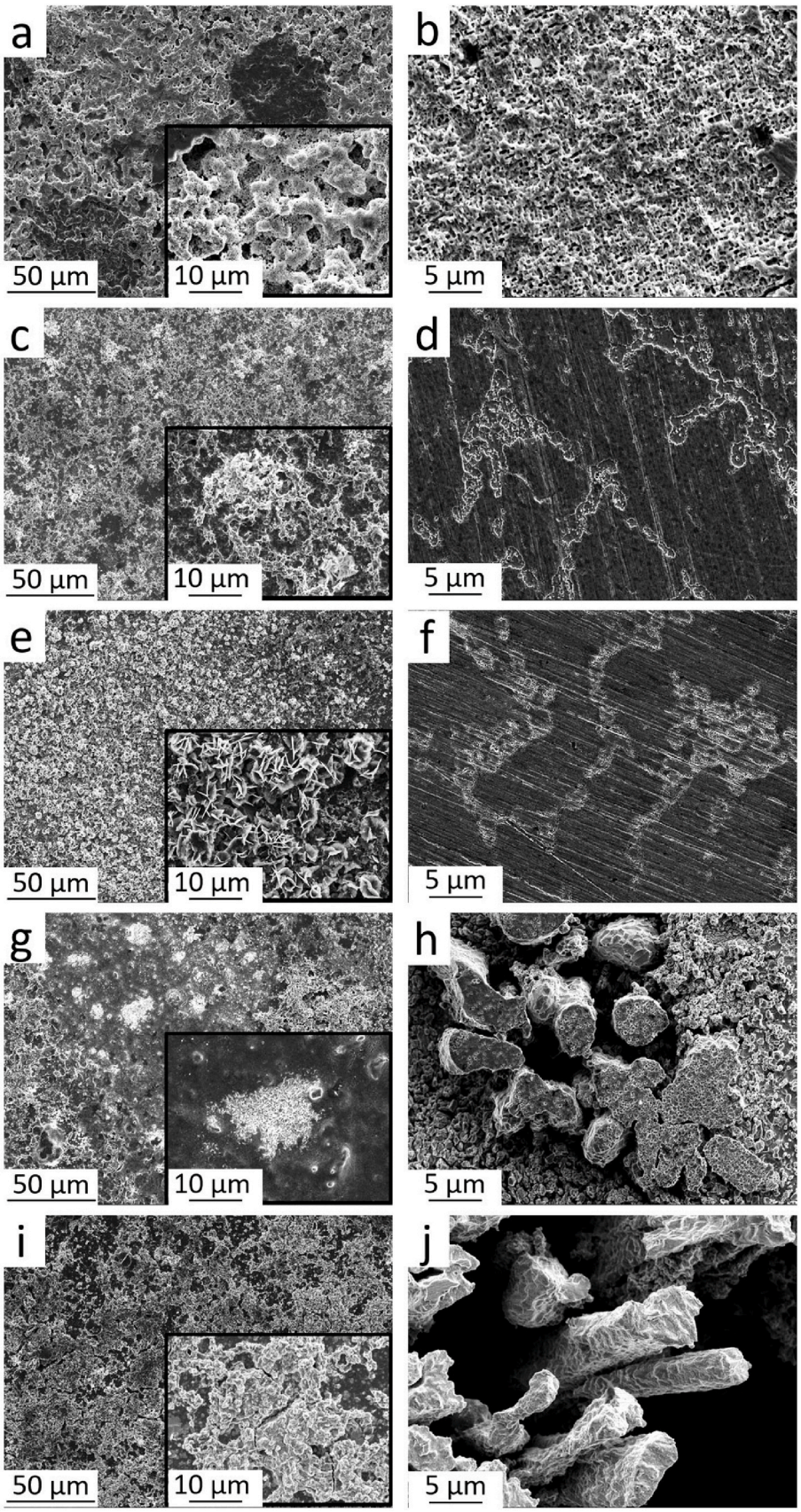

Fig. 6. SEM images of the corroded samples after 10 days of immersion in Hanks' solution at 37 °C, before (left column) and after (right column) the removal of the corrosion products: Zn (a, b), Zn-0.5Mg (c, d), Zn-1Mg (e, f), Zn-3Cu (g, h), and Zn-5Cu (i, j).

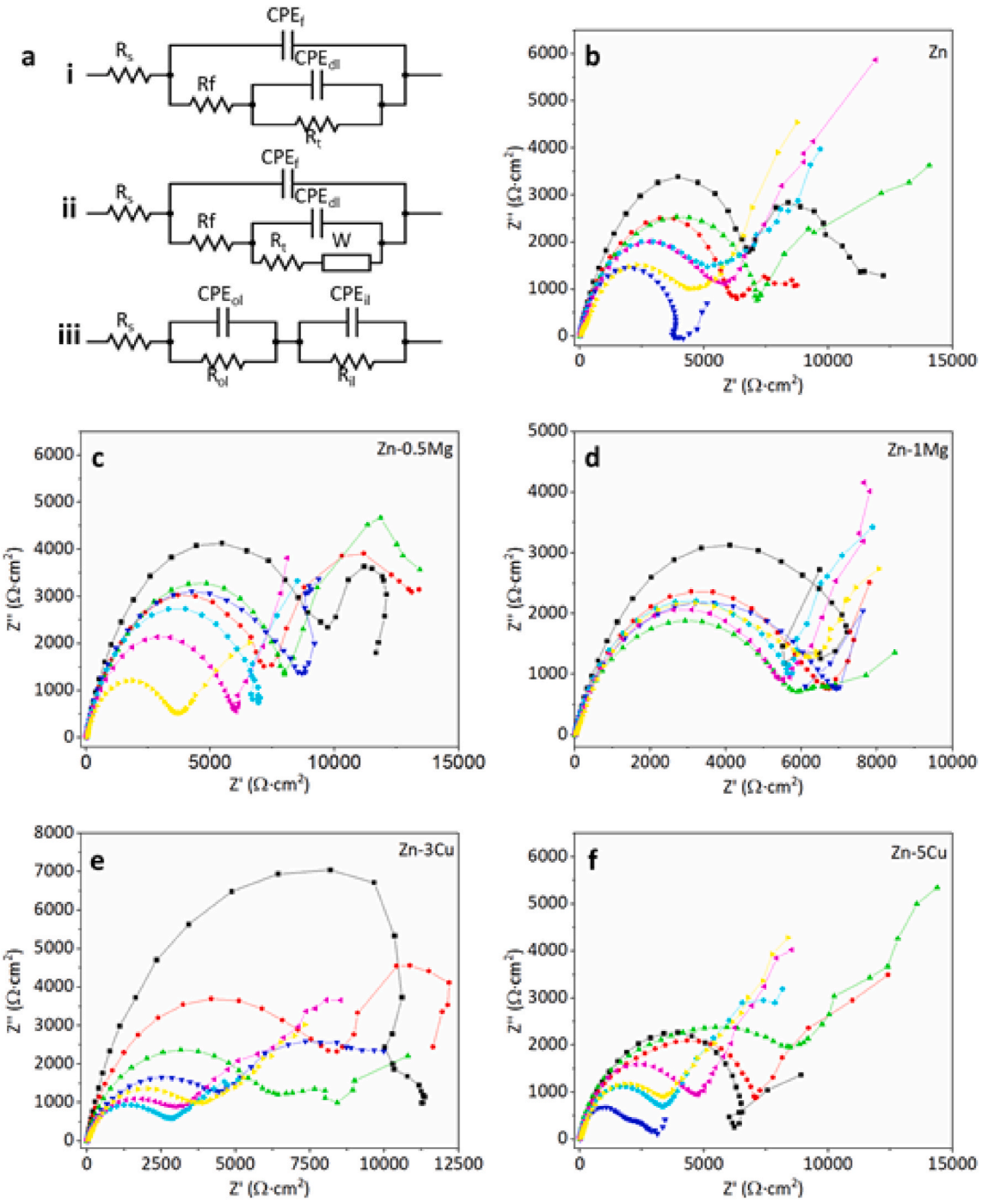

Fig. 7. Electrochemical impedance spectroscopy (EIS) evaluation in Hanks' solution of Zn and Zn-based alloys: (a) Equivalent circuits of (i) passivation layer, (ii) porous layer, and (iii) bi-layer model. EIS Nyquist plots: (b) Zn, (c) Zn-0.5Mg, (d) Zn-1Mg, (e) Zn-3Cu, and (f) Zn-5Cu. Time after immersion: ●-2h, ●-4h, ▲-8h, ▼-26h, ◆-2d, ◀-3d, and ▶-7d.

studies with *P. aeruginosa* showed that morphology remained intact after the culturing. Similar bacteria adhesion is observed for pure Zn, Zn-0.5Mg, and Zn-1Mg alloys (Fig. 8b, d, f, respectively). The number of bacteria adhered on the Zn-Cu alloys surfaces were lower in comparison to pure Zn (Fig. 8h, j). Additionally, it was observed surface morphology changes of Zn and Zn-Mg alloys after incubation with *P. aeruginosa.* SEM images showed that *P. aeruginosa* adhesion was higher onto degraded areas of Zn and Zn-Mg alloys compared to smoother parts (Fig. 8b, d, f). No adhered bacteria were found onto non-degraded Zn-5Cu surface (Fig. 8j).

3.6. Endothelial cell response

3.6.1. Indirect contact cytotoxicity

Fig. 9 shows the results from cytotoxicity assays by indirect contact of HAoEC with metal extracts obtained from incubating alloys discs for 3

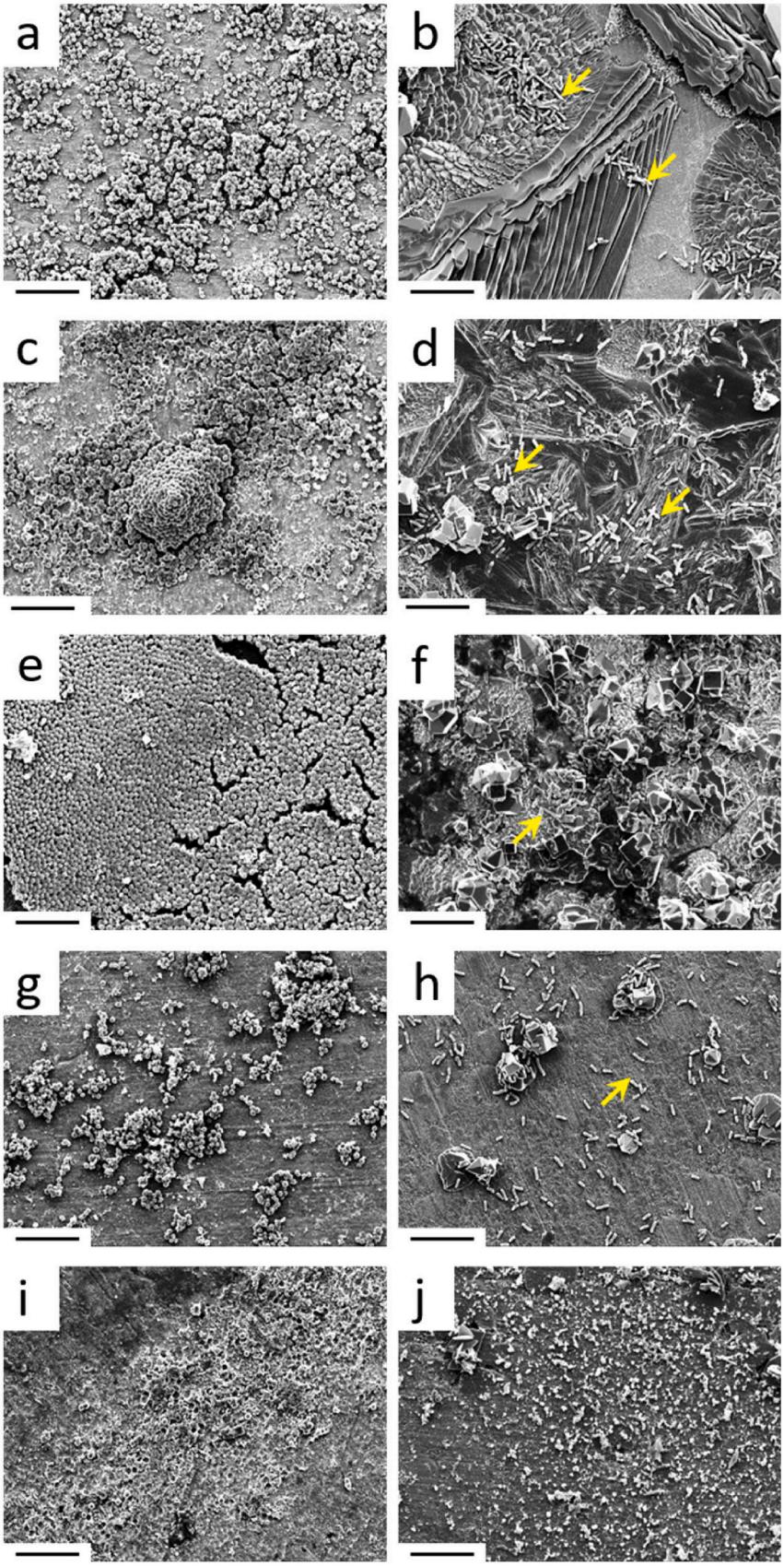

Fig. 8. SEM images of bacterial morphology for both *S. aureus* (left) and *P. aeruginosa* (right) after culturing for 2 h on pure Zn (a, b), Zn-0.5Mg (c, d), Zn-1Mg (e, f), Zn-3Cu (g, h), and Zn-5Cu (i, j). Scale bar: 20 μm. Yellow arrows indicate *P. aeruginosa* bacteria.

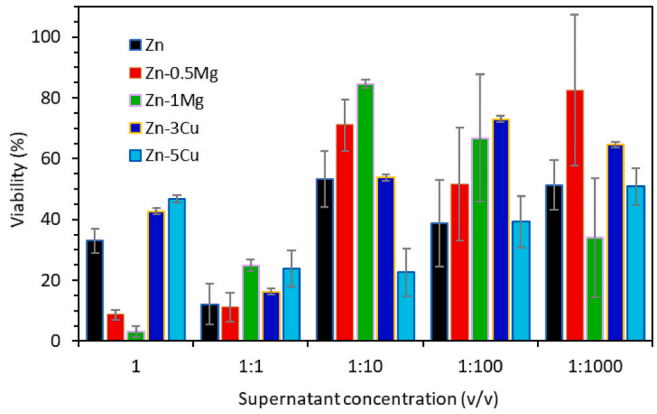

Fig. 9. Indirect HAoEC viability after 24 h of culture in supernatants prepared by immersion of the alloys in Growth Medium for 3 days. Aliquots of supernatants at decreased concentrations were added to adhered cells.

days in Growth Medium. Viability results suggested that Zn and the here studied alloys are cytotoxic to HAoEC. According to the ISO 10993-5 [45], a cell viability reduction larger than 30% is considered as cytotoxic. Since we measure viability as a ratio to the positive control group, a value below 70% indicates cytotoxicity. This was the case of cells cultured in undiluted and 50% diluted extracts. For diluted extracts below 1:10 v/v, there was not an evident cytotoxic effect, particularly in the case of Zn-Mg alloys. Among the alloys with Cu content, the results suggested cytotoxicity of Zn-5Cu.

3.6.2. *HAoEC viability by direct contact*

HAoEC adhesion/proliferation of the cells were evaluated at day 1, day 3 and day 7. Fig. 10 summarizes the results for all alloys including pure Zn. In general, all materials showed poor cell adhesion with viability values below 30% after day 1. After 3 and 7 days, there was a prominent decrease in HAoEC population particularly on Zn-Cu alloys.

To further investigate cytotoxicity effects, cell morphologies in direct contact with the alloys were observed with SEM at day 1, day 3 and day 7, and cell distribution was determined at day 7 by confocal microscopy. Representative images of HAoEC morphologies on the different materials are depicted in Fig. 11. Cells exhibited spread morphology on Zn (Fig. 11a–c) and Zn-0.5Mg (Fig. 11e–g) throughout the immersion period. This morphology was an indication of good cell adhesion to the surface; however, cell population showed to be low as observed from live/dead confocal images of both Zn (Fig. 11d) and Zn-0.5Mg (Fig. 11h). This was in accordance to cell viability results in Fig. 10. In the case of Zn-1Mg and Zn-Cu alloys (Fig. 11i, m, q), HAoEC tended to gather in bundles. In the case of healthy cells, such bundles might be an indication of local cell proliferation. However, it is probably not the current case. Anchorage dependent cells attach to each other to survive when they are not able to attach to the underlying surface.

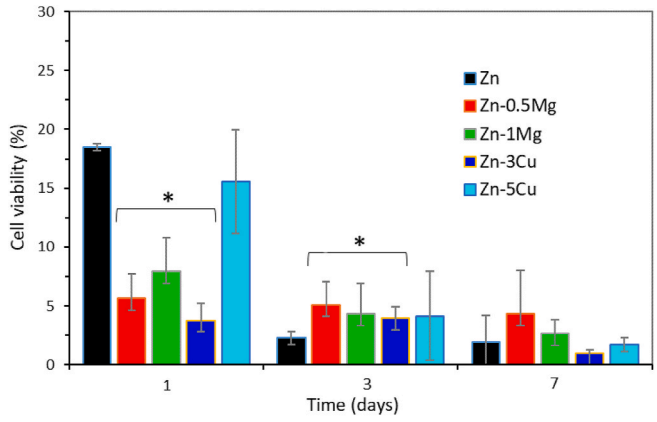

Fig. 10. Cell viability of HAoEC seeded on the alloys measured by LDH test. (*) Statistically significant differences in comparison to Zn control group, $P < 0.05$.

Formation of localized corrosion products was observed for Zn-1Mg (Fig. 11j and k) and both Zn-Cu (Fig. 11n-o, r-s) alloys at day 3 and day 7, respectively, in contrast to a rather smooth corrosion layer observed at day 1 for all materials. In general, cell viability results (Fig. 10) agreed with cell morphology observations with SEM and dead/live confocal microscopy images. HAoEC adhesion and proliferation on the here studied Zn alloys and conditions, is negligible.

4. Discussion

Among bioresorbable metals, Zn and its alloys are becoming popular as part of the next generation of temporary implant materials that potentially prevent complications related to the use of permanent metals. From the mechanical point of view, Zn alloys have shown to have potential for cardiovascular stents. The requirements for cardiovascular stents include suitable stiffness that provide radial support to help restore the blood flow [56,57]; avoiding cracking during crimping and reinflation in order to prevent early loss of mechanical integrity; fatigue resistance to endure the stretching during cyclic heart contractions; and durability to avoid fracture that may lead to in-stent thrombosis [58].

The degradation rate, degradation products and biocompatibility are also key properties. Ideally, the degradation rate of a bioresorbable vascular stent should be about 20 μm/year to prevent excessive accumulation of degradation products that can cause long-term symptoms [59]. Unalloyed Zn has an appropriate degradation rate for cardiovascular stents application in comparison to Mg- and Fe-based alloys. Moreover, it is also an essential element for healthy bones, muscles and liver. However, the mechanical properties are lower compared to metallic materials used for commercial BMS. The addition of alloying elements such as Mg and Cu has been reported to effectively refine the microstructure of Zn [34]. Moreover, extrusion process may modify the texture of alloyed Zn showing grain texture which also may influence the mechanical properties [60].

As expected, the microstructure of Zn-Mg alloys consisted of a primary α-Zn dendritic grains along with a Zn + Mg_2Zn_{11} eutectic, mainly located at grain boundaries (Fig. 1c–f) [61]. The reason is that Zn-Mg phase diagram shows a maximum of Mg solubility in Zn of 0.1 wt% at 364 °C [62], consistent with the results reported by Li [63], Prosek [64] and Yao [65]. Fig. 1e shows the eutectic phase surrounding the grains of 30 μm size, suggesting a refinement of the microstructure by alloying. The microstructure of the longitudinal sections showed Zn grains and the eutectic phase elongated to the rolling direction (Fig. 1d,f). Zn-Cu phase diagram indicates a peritectic reaction where a Cu content between 2.7 and 22 wt % results in the formation of a two-phase alloy consisting of a primary ε-$CuZn_5$ dendrites and Zn matrix [62,66,67].

The addition of Mg as an alloying element enhanced the mechanical properties of pure Zn. In fact, among the tested materials, Zn-1Mg the highest YS and UTS (Fig. 2). The limited elongation of Zn-1Mg alloy is due to the interconnected network of Zn + Mg_2Zn_{11} eutectic phase (Fig. 1e), which facilitates the growth of fracture cracks before the onset of plastic strain [18]. The statistically higher plasticity of Zn-0.5Mg is due to the absence of a continuous network (Fig. 1c). On the other hand, Zn-Cu alloys showed a larger elongation compared to Zn and Zn-Mg alloys. Superplastic behavior (>400% fracture elongation) has been previously reported for Zn-Cu alloys with Cu content below 1 wt%, with preferential sliding at Zn/ε-$CuZn_5$ interphase rather than at Zn/Zn grain boundaries [68,69]. The obtained lower values can be attributed to the grain size and to the non-homogeneous distribution of ε-$CuZn_5$ intermetallic phase. The higher volume fraction of the secondary phases in both Zn-Mg and Zn-Cu alloys increased the final mechanical properties, as confirmed by nanoindentation results. The extremely low solubility of

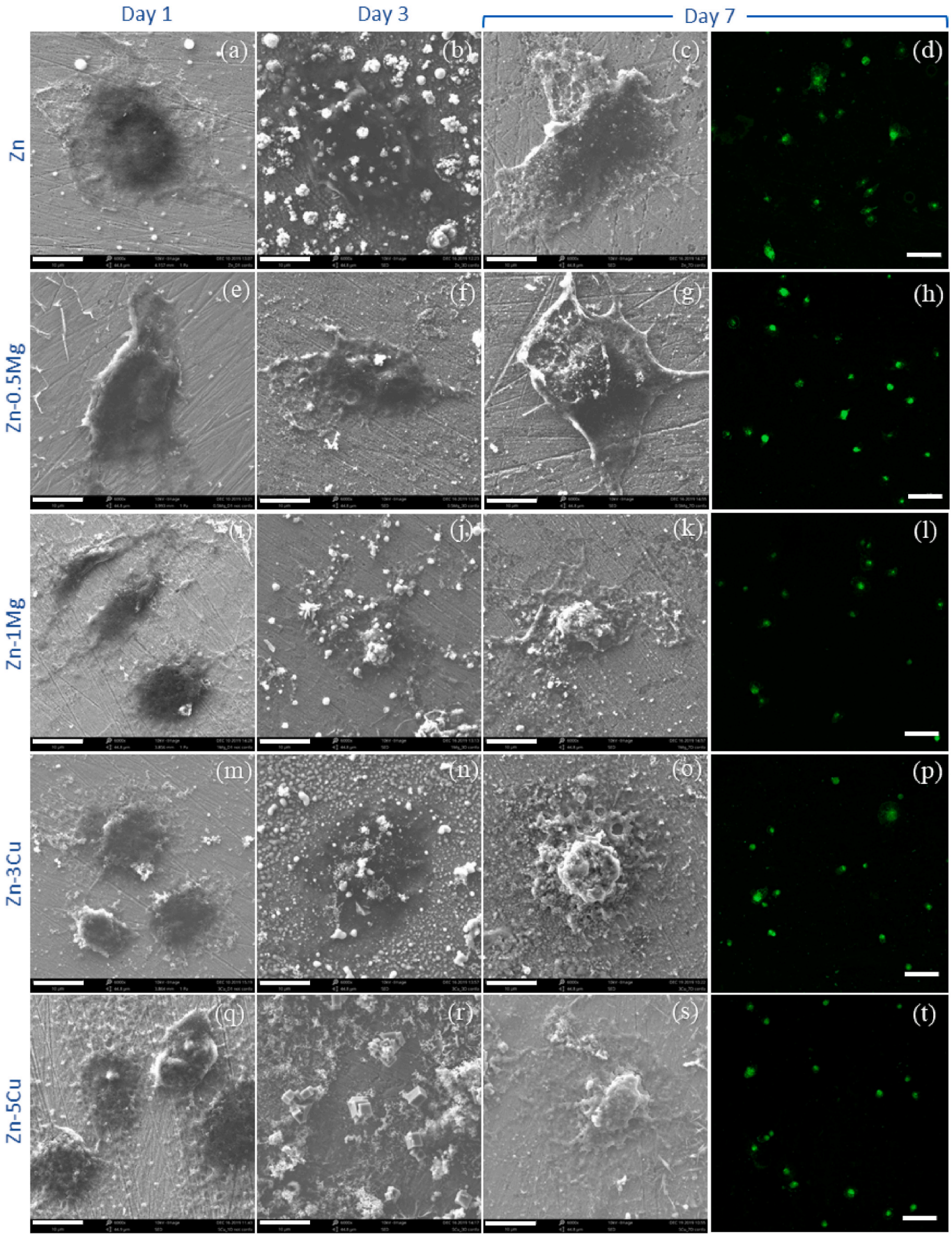

Fig. 11. SEM (scale bar 10 μm) and confocal (scale bar 100 μm) images of HAoEC morphology and distribution after 1 day (left hand column), 3 days (2nd column) and 7 days (right hand 2 columns) of culturing on Zn (a)–(d), Zn-0.5Mg (e)–(h), Zn-1Mg (i)–(l), Zn-3Cu (m)–(p), and Zn-5Cu (q)–(t).

Mg in the Zn matrix (0.1 wt%) [62] was enough to increase the hardness of Zn matrix. Similarly, the Cu dissolved into Zn matrix (2.75 wt%) [62] reduces its hardness. As seen in Table 2, the secondary phases manifested statistically larger hardness in comparison to Zn matrix, 2.6 GPa for Zn + Mg_2Zn_{11} and 1.82 GPa for ε-$CuZn_5$, confirming that the presence of secondary phases enhances the macroscopic mechanical properties of Zn (Fig. 2a).

The anodic and catodic reactions involved in the corrosion mechanism of bioresorbable Zn-based alloys are summarized in Eqs (4)–(8). The released electrons from the oxidation of the metal (Eq. (4)) are involved in cathodic processes as the reduction of protons from water molecules (Eq. (5)) or the reduction of O_2(g) (Eq. (6)). Both cathodic reactions produce hydroxide ions increasing the pH of the solution and that could promote the formation of zinc hydroxides ($Zn(OH)_2$(s)) (Eq. (7)) or zinc oxide (ZnO(s)) (Eq. (8)).

$$Zn(s) \rightarrow Zn^{2+}(aq) + 2e^- \text{ (anodic reaction)} \quad (4)$$

$$2H_2O + 2e^- \rightarrow H_2(g) + 2OH^-(aq) \text{ (cathodic reaction)} \quad (5)$$

$$2H_2O + O_2(g) + 4e^- \rightarrow 4OH^-(aq) \text{ (cathodic reaction)} \quad (6)$$

$$Zn^{2+} + 2OH^- \rightarrow Zn(OH)_2(s) \text{ (by-product formation)} \quad (7)$$

$$Zn^{2+} + H_2O \rightarrow ZnO(s) + 2H^+ \text{ (by-product formation)} \quad (8)$$

This is a simplified model where it has not been considered the influence of other major species present in Hanks' solution, chloride, bicarbonate and phosphate ions. These ions are potentially responsible for the formation of chloride, carbonate and phosphate minerals as it is described in Eqs. (9)–(11).

$$Zn^{2+} + 2Cl^- \rightarrow ZnCl_2(s) \text{ (by-product formation)} \quad (9)$$

$$Zn^{2+} + HCO_3^- \rightarrow ZnCO_3(s) + 2H^+ \text{ (by-product formation)} \quad (10)$$

$$3Zn^{2+} + 2HPO_4^{-2} \rightarrow Zn_3PO_4(s) + 2H^+ \text{ (by-product formation)} \quad (11)$$

Oxidation-reduction reactions involve electron exchanges that require optimal balance for proper cell function. Enzymes as superoxide dismutase (SOD) and catalase act as redox buffers modulating different cellular processes. Redox homeostasis is governed by the presence of these antioxidants that absorb and buffer reductants and oxidants [48,70]. Under optimal cellular conditions, SOD and catalase are maintained in a highly reduced state (E < 0 V) and buffer the reactive oxygen species (ROS). A redox misbalance could transform the superoxide anion ($O_2^{\cdot-}$) to hydrogen peroxide (H_2O_2) (E, $O_2^{\cdot-}/H_2O_2$ = +0.94 V). The subsequent reduction of H_2O_2 produces the hydroxyl radical ($OH^{\cdot}$) (E, $H_2O_2/OH^{\cdot}$ = +0.54 V), an extremely reactive electron and hydrogen acceptor whose reduction potentially comprises unselective oxidation of cellular components as the lipids present in the lipidic bilayers, amino acids, or DNA [71]. Indeed, oxidative stress have been demonstrated to be related to atherosclerosis [72]. The degradation of studied Zn and Zn alloys occurred at negative redox potentials without subjecting cells to oxidative stress.

Pourbaix diagrams for Zn-Mg and Zn-Cu alloys in Hanks' modified solution at 37 °C were calculated using HSC 5.1 Software (Fig. S7). At the measured pH and E values, the expected species for Zn^{2+} are $ZnCO_3$/ZnO (Fig. S7a); for Mg^{2+}: Mg^{2+}/MgO (Fig. S7b), and for Cu^{2+}: Cu/Cu_2O (Fig. S7c) According to Pourbaix diagrams of Fig. S7c, it is not expected any oxidized form of Cu as Cu^{2+} which is in agreement with the non-detection of Cu^{2+}, values were below the detection limit (<0.01 μg/dL). On the contrary, Fig. S7a, suggested to expect very low concentrations of Zn^{2+} in these conditions. However, it should be pointed out that Pourbaix diagrams provide a thermodynamic prediction and it should be added the integration of the kinetics of the different processes (Eqs. (4)–(10)) describing the degradation mechanism of Zn and Zn alloys.

Regarding the corrosion degradation properties, the corrosion products layer formed on both Zn-Mg alloys demonstrated to be more protective to Zn than the corrosion layers of Zn-Cu alloys. Zn-1Mg showed the better performance in terms of corrosion layer stability and protection in Hanks' solution under the studied conditions. Some studies have reported that this is due to the presence of magnesium hydroxyl carbonate ($Mg(OH)(HCO_3)$(s)) that improve the corrosion resistance of Zn-based alloys as it is electrochemically inert in aqueous solutions [62]. Zn-1Mg alloy also showed the highest current density among the tested materials. The larger amount of fine intermetallic Zn + Mg_2Zn_{11} in the microstructure, results in a higher number of galvanic couples, which may explain the higher current density value. Immersion test stated that the total released Zn^{2+} concentration is within the levels of Zn^{2+} in blood (60–240 μg/dL) [49,50]. Another challenge associated to cardiovascular stents is the platelet adhesion and thereby blood clotting. A strategy for the inhibition of the coagulation cascade is the control of the wettability, which could inhibit the adsorption of specific proteins and, thereby, promote hemocompatibility [73,74]. Moreover, the higher hydrophobicity is directly related to a better corrosion resistance [73,74]. Therefore, the values obtained suggested that Cu addition to Zn matrix increases the corrosion resistance of Zn. The hydrophilicity of Zn-1Mg alloy suggested a lower corrosion resistance of Zn, which is in accordance with the highest current density value reported in PDP studies (Table 3) and the galvanic couples homogeneously distributed (Fig. 6d,f).

Bacterial activity is related to the kinetics of degradation as well as the nature of the degradation products. Cu is an antibacterial agent and the minimum inhibitory concentration (MIC) needed is 100 mg/L [75]. According to the results of the immersion test, the detected concentration of Cu^{2+} was below 0.01 mg/L. However, it must be pointed out the different conditions established for both experiments: immersion test comprises the total immersion of the materials into inorganic Hanks' solution; whereas in the agar diffusion test the samples are deposited onto the agar plate with BHI. Hence, it is hypothesized that Cu^{2+} dissolved into the Zn matrix in Zn-Cu alloys may diffuse with the degradation of the material at this primary stage, leading to an antibacterial effect for *S. aureus* controlled by diffusion mechanisms [76]. Cu^{2+} cations are often introduced to render antimicrobial properties to inert materials. Different antibacterial mechanisms based on Cu^{2+} diffusion have been reported. Cu^{2+} cations can interact with microbial membrane and alter their structure and permeability, or they can prevent microbial replication via interaction with microbial nucleic acids [1,28–30]. *Pseudomonas* have been used as metal resistant strains capable of bioaccumulation of multiple metals as zinc or copper and their dissolution [77]. Bacterial SEM images suggested that *P. aeruginosa* stimulates the degradation of Zn and Zn-Mg alloys under studied conditions modifying the chemical composition of the surface and its morphology. Moreover, the results showed a preferential adhesion of *P. aeruginosa* bacteria onto the degraded and rougher areas compared to non-degrades and smoother ones. Thus, controlling the degradation products and consequent roughness of BRS is also critical for avoiding bacterial infection [78].

Zn and its alloys indicated a deficient *in vitro* biocompatibility, however *in vivo* studies have shown positive results [16,17,20]. Shearier et al. [17] discussed two reasons for this: (i) the formation of a confluent protein layer over the material surface, that occurs *in vivo,* avoids the cells to be in direct contact with the implant surface; and (ii) the blood flow might help to alleviate the local concentration of cytotoxic ions or degradation products that may be harmful for cells. The absence of these conditions *in vitro* might lead to local high Zn^{2+} ions concentration that promotes cell dead [17]. This hypothesis is in accordance with the viability results in Fig. 10. The longer the incubation time of the cells in direct contact with the metallic surfaces, the lower the viability values were observed. Besides the exposure to local high Zn^{2+} ion concentration, cells are also exposed to degradation products that might also be cytotoxic. The nature and morphology of these corrosion products certainly impacted cell viability and, as shown in Fig. 10, cells are in

direct contact with these degradation products. HAoEC rounded shape surrounded by either corrosion products, is characteristic of weak cell adhesion. Once upon immersion, Zn degradation starts with oxidation processes releasing Zn^{2+} cations to the aqueous solution. Li *et al.* [79] reported there is an apparent lethal dose depending on the cell type. Human aortic endothelial cells showed to be more resilient to the presence of Zn^{2+} in comparison to human aortic smooth muscle cells and human dermal fibroblasts [79]. Previous studies [62,80] have also reported a toxic effect for undiluted extracts in standard ISO 10993-5/12 test. Moreover, significant differences of cytotoxicity results among different studies have been also reported. It is important to remark that the ISO standards 10993-5/12 were originally developed for biocompatibility evaluation of inert materials. Due to their traditional use and simplicity of implementation, these standards were rapidly adopted for screening biocompatibility of bioresorbable materials. However, cytotoxicity is affected by degradation products released from the materials and sensitive to different extraction vehicles [79]. According to Li *et al.*, cytotoxicity results are directly affected by three main factors: alloy nature, cell line used and the extraction condition [79]. As stated by Li *et al.* [79], the medium and conditions of extraction influence the outcome of standardized *in vitro* cytotoxicity tests. In the same way, Wang *et al.* [81] recommend a minimal of 6 times to maximum 10 times dilution extracts since *in vitro* data should match *in vivo* data for cytotoxicity tests. However, still for HAoEC type Zn alloys inhibitory effect on cell viability confirms the need of functionalize Zn alloys surface intended for biomedical applications.

In general, Zn-based materials showed high potential to be used as BRS. As proven, their mechanical properties and degradation rate can be adjusted by alloying with Mg and Cu. However, cell adhesion and proliferation still need significant improvement. Therefore, future work should be focused on surface functionalization of these alloys in order to achieve the desired *in vitro* and *in vivo* biocompatibility.

5. Conclusions

In this study, mechanical, corrosion and biocompatible properties of Zn, Zn-0.5Mg, Zn-1Mg, Zn-3Cu, and Zn-5Cu alloys were thoroughly characterized in order to select an adequate material for stenting applications. Tensile mechanical testing and Vickers assays confirmed that alloying with Mg or Cu alloying significantly increased YS and UTS of Zn. This is due to the formation of hard Zn + Mg_2Zn_{11} and ε-$CuZn_5$ secondary phases on Zn-Mg and Zn-Cu alloys, respectively, as determined by nanoindentation tests. Nanoindentation tests determined the hardness and elastic modulus of the matrix and the secondary phases of the studied alloys. Fractured surfaces images were in accordance to tensile tests results showing the differences in grain size among the tested materials. Potentiodynamic results indicated that the corrosion layer of Zn-Mg is more protective than the formed onto Zn-Cu alloys, also confirmed by the nyquist spectra from EIS measurements. Impedance and polarization results showed that the corrosion mechanisms consisted of galvanic corrosion followed by the formation of an inner corrosion layer plus local precipitation of compounds rich in Ca, C, O, P, and Cl. Static immersion assay in Hanks' modified solution indicated Zn^{2+} released values within normal blood levels, Mg^{2+} release was 10 μg/dL, and Cu^{2+} was not detected by ICP-MS. The formation of these compounds and the Zn^{2+} release compromises the adhesion and proliferation of HAoECs in tested conditions. Cytotoxicity assays suggested that such products are cytotoxic to HAoECs. *S. aureus* showed to be more resilient to Zn-Mg alloys, different from this strain on Zn-Cu alloys evidenced by diffusion and adhesion tests. In vitro tests proved the need of functionalizing Zn-Mg and Zn-Cu alloys for the intended application. Among the tested materials, Zn-1Mg showed the best compromise in mechanical and degradation properties for cardiovascular stents.

CRediT authorship contribution statement

García-Mintegui Claudia: Investigation, Methodology, Writing – original draft. **Córdoba Laura Catalina:** Investigation, Methodology, Writing – original draft. **Buxadera-Palomero Judit:** Investigation. **Marquina Andrea:** Investigation. **Jiménez-Piqué Emilio:** Validation. **Ginebra Maria-Pau:** Supervision, Funding acquisition. **Cortina José Luís:** Supervision, Validation. **Pegueroles Marta:** Writing – review & editing, Supervision, Formal analysis, Funding acquisition.

Declaration of competing interest

The authors declare no conflict of interest.

Acknowledgements

Financial support was received from Spanish Government, MINECO/FEDER, (RTI2018-098075-B-C21) and the Agency for Administration of University and Research Grants of the Government of Catalonia (2017SGR-1165). L.C.C. thanks COFUND scheme (GA 712754) and SEV-2014-0425 (2015–2019) for the financial support. Support for the research of M-P.G. was received through the prize "ICREA Academia" for excellence in research, funded by the Generalitat de Catalunya. Authors acknowledge Dr. Daniel Rodríguez-Rius for helping in the corrosion studies and measurement setup.

Appendix A. Supplementary data

Supplementary data to this article can be found online at https://doi.org/10.1016/j.bioactmat.2021.04.015.

References

[1] H.M.M. van Beusekom, P.W. Serruys, Drug-eluting stent endothelium. Presence or dysfunction, JACC Cardiovasc. Interv. 3 (2010) 76–77, https://doi.org/10.1016/j.jcin.2009.10.016.
[2] P. Ramadugu, K. Latha Alikatte, A review on biodegradable and bioabsorbable stents for coronary artery disease, J. Bioequiv. 8 (2016) 64–67, https://doi.org/10.4172/jbb.1000269.
[3] Y.F. Zheng, X.N. Gu, F. Witte, Biodegradable metals, Mater. Sci. Eng. R. 77 (2014) 1–34, https://doi.org/10.1007/978-1-4614-3942-4_5.
[4] Y. Sotomi, Y. Onuma, C. Collet, E. Tenekecioglu, R. Virmani, N.S. Kleiman, P. W. Serruys, Bioresorbable scaffold: the emerging reality and future directions, Circ. Res. 120 (2017) 1341–1352, https://doi.org/10.1161/CIRCRESAHA.117.310275.
[5] M. Prakasam, J. Locs, K. Salma-Ancane, D. Loca, A. Largeteau, L. Berzina-Cimdina, Biodegradable materials and metallic implants—a review, J. Funct. Biomater. 8 (2017) 44, https://doi.org/10.3390/jfb8040044.
[6] H.S. Han, S. Loffredo, I. Jun, J. Edwards, Y.C. Kim, H.K. Seok, F. Witte, D. Mantovani, S. Glyn-Jones, Current status and outlook on the clinical translation of biodegradable metals, Mater. Today 23 (2019) 57–71, https://doi.org/10.1016/j.mattod.2018.05.018.
[7] M. Moravej, D. Mantovani, Biodegradable metals for cardiovascular stent application: interests and new opportunities, Int. J. Mol. Sci. 12 (2011) 4250–4270, https://doi.org/10.3390/ijms12074250.
[8] R. Song, M. Murphy, C. Li, K. Ting, C. Soo, Z. Zheng, Current development of biodegradable polymeric materials for biomedical applications, Drug Des. Dev. Ther. 12 (2018) 3117–3145, https://doi.org/10.2147/DDDT.S165440.
[9] A. Purnama, H. Hermawan, D. Mantovani, Biodegradable metal stents: a focused review on materials and clinical studies, J. Biomater. Tissue Eng. 4 (2015) 868–874, https://doi.org/10.1166/jbt.2014.1263.
[10] D. Zhao, F. Witte, F. Lu, J. Wang, J. Li, L. Qin, Current status on clinical applications of magnesium-based orthopaedic implants: a review from clinical translational perspective, Biomaterials 112 (2017) 287–302, https://doi.org/10.1016/j.biomaterials.2016.10.017.
[11] P.C. Banerjee, S. Al-Saadi, L. Choudhary, S.E. Harandi, R. Singh, Magnesium implants: prospects and challenges, Materials 12 (2019) 1–21, https://doi.org/10.3390/ma12010136.
[12] D. Pierson, J. Edick, A. Tauscher, E. Pokorney, P. Bowen, J. Gelbaugh, J. Stinson, H. Getty, C.H. Lee, J. Drelich, J. Goldman, A simplified in vivo approach for evaluating the bioabsorbable behavior of candidate stent materials, J. Biomed. Mater. Res. B Appl. Biomater. 100 B (2012) 58–67, https://doi.org/10.1002/jbm.b.31922.
[13] D. Vojtěch, J. Kubásek, J. Šerák, P. Novák, Mechanical and corrosion properties of newly developed biodegradable Zn-based alloys for bone fixation, Acta Biomater. 7 (2011) 3515–3522, https://doi.org/10.1016/j.actbio.2011.05.008.

[14] M.I. Rahim, S. Ullah, P.P. Mueller, Advances and challenges of biodegradable implant materials with a focus on magnesium-alloys and bacterial infections, Metals 8 (2018), https://doi.org/10.3390/met8070532.
[15] C. Li, C. Guo, V. Fitzpatrick, A. Ibrahim, M.J. Zwierstra, P. Hanna, A. Lechtig, A. Nazarian, S.J. Lin, D.L. Kaplan, Design of biodegradable, implantable devices towards clinical translation, Nat. Rev. Mater. 5 (2020) 61–81, https://doi.org/10.1038/s41578-019-0150-z.
[16] P.K. Bowen, J.W. Drelich, J. Goldman, Zinc exhibits ideal physiological corrosion behavior for bioabsorbable stents, Adv. Mater. 25 (2013) 2577–2582, https://doi.org/10.1002/adma.201300226.
[17] E.R. Shearier, P.K. Bowen, W. He, A. Drelich, J. Drelich, J. Goldman, F. Zhao, In vitro cytotoxicity, adhesion, and proliferation of human vascular cells exposed to zinc, ACS Biomater. Sci. Eng. (2016), https://doi.org/10.1021/acsbiomaterials.6b00035.
[18] J. Kubásek, D. Vojtěch, E. Jablonská, I. Pospíšilová, J. Lipov, T. Ruml, Structure, mechanical characteristics and in vitro degradation, cytotoxicity, genotoxicity and mutagenicity of novel biodegradable Zn–Mg alloys, Mater. Sci. Eng. C 58 (2016) 24–35, https://doi.org/10.1016/j.msec.2015.08.015.
[19] W.M.P.F. Bosman, B.L.S. Borger Van Der Burg, H.M. Schuttevaer, S. Thoma, P. P. Hedeman Joosten, Infections of intravascular bare metal stents: a case report and review of literature, Eur. J. Vasc. Endovasc. Surg. 47 (2014) 87–99, https://doi.org/10.1016/j.ejvs.2013.10.006.
[20] G. Katarivas Levy, J. Goldman, E. Aghion, The prospects of zinc as a structural material for biodegradable implants—a review paper, Metals 7 (2017) 402, https://doi.org/10.3390/met7100402.
[21] G. Katarivas Levy, A. Leon, A. Kafri, Y. Ventura, J.W. Drelich, J. Goldman, R. Vago, E. Aghion, Evaluation of biodegradable Zn-1%Mg and Zn-1%Mg-0.5%Ca alloys for biomedical applications, J. Mater. Sci. Mater. Med. 28 (2017) 1–11, https://doi.org/10.1007/s10856-017-5973-9.
[22] Z. Tang, H. Huang, J. Niu, L. Zhang, H. Zhang, J. Pei, J. Tan, G. Yuan, Design and characterizations of novel biodegradable Zn-Cu-Mg alloys for potential biodegradable implants, Mater. Des. 117 (2017) 84–94, https://doi.org/10.1016/j.matdes.2016.12.075.
[23] D. Persaud-Sharma, N. Budiansky, In Vitro Degradation Behavior of Ternary Mg-Zn-Se and Mg-Zn-Cu Alloys as Biomaterials, vol. 193, 2011, pp. 118–125, https://doi.org/10.1016/j.jneumeth.2010.08.011.Autogenic.
[24] B. Jia, Z. Zhang, X. Qu, W. Lin, Alloying design of biodegradable zinc as promising bone implants for load-bearing applications, Nat. Commun. (2020) 1–16, https://doi.org/10.1038/s41467-019-14153-7.
[25] Y. Zhang, Y. Yan, X. Xu, Y. Lu, L. Chen, D. Li, Y. Dai, Y. Kang, K. Yu, Investigation on the microstructure, mechanical properties, in vitro degradation behavior and biocompatibility of newly developed Zn-0.8%Li-(Mg, Ag) alloys for guided bone regeneration, Mater. Sci. Eng. C 99 (2019) 1021–1034, https://doi.org/10.1016/j.msec.2019.01.120.
[26] C. Xiao, L. Wang, Y. Ren, S. Sun, E. Zhang, C. Yan, Q. Liu, X. Sun, F. Shou, J. Duan, H. Wang, G. Qin, Indirectly extruded biodegradable Zn-0.05wt%Mg alloy with improved strength and ductility: in vitro and in vivo studies, J. Mater. Sci. Technol. 34 (2018) 1618–1627, https://doi.org/10.1016/j.jmst.2018.01.006.
[27] H. Yang, B. Jia, Z. Zhang, X. Qu, G. Li, W. Lin, D. Zhu, K. Dai, Y. Zheng, Alloying design of biodegradable zinc as promising bone implants for load-bearing applications, Nat. Commun. 11 (2020) 1–16, https://doi.org/10.1038/s41467-019-14153-7.
[28] A.W. Feinberg, W.R. Wilkerson, C.A. Seegert, A.L. Gibson, L. Hoipkemeier-Wilson, A.B. Brennan, Systematic variation of microtopography, surface chemistry and elastic modulus and the state dependent effect on endothelial cell alignment, J. Biomed. Mater. Res. 86 (2008) 522–534, https://doi.org/10.1002/jbm.a.31626.
[29] J.A. Ormiston, M.W.I. Webster, Trial Data and the Real World, 2015, pp. 1–4, https://doi.org/10.4244/EIJY15M02.
[30] H. Pourabolghasem, M. Ghorbanpour, R. Shayegh, Antibacterial activity of copper-doped montmorillonite nanocomposites prepared by alkaline ion exchange method, J. Phys. Sci. 27 (2016) 1–12, https://doi.org/10.21315/jps2016.27.2.1.
[31] E.D. Harris, A requirement for copper in angiogenesis, Nutr. Rev. 62 (2004) 60–64, https://doi.org/10.1301/nr.2004.feb.60.
[32] C. Giacomelli, M.L. Trincavelli, C. Satriano, Ö. Hansson, D. La Mendola, E. Rizzarelli, C. Martini, Copper (II) ions modulate Angiogenin activity in human endothelial cells, Int. J. Biochem. Cell Biol. 60 (2015) 185–196, https://doi.org/10.1016/j.biocel.2015.01.005.
[33] L. Finney, S. Vogt, T. Fukai, D. Glesne, Copper and angiogenesis: unravelling a relationship key to cancer progression, Clin. Exp. Pharmacol. Physiol. 36 (2009) 88–94, https://doi.org/10.1111/j.1440-1681.2008.04969.x.
[34] Z. Liu, F. Wang, D. Qiu, J.A. Taylor, M. Zhang, The effect of solute elements on the grain refinement of cast Zn, Metall. Mater. Trans. A Phys. Metall. Mater. Sci. 44 (2013) 4025–4030, https://doi.org/10.1007/s11661-013-1861-1.
[35] W. Bednarczyk, M. Wątroba, J. Kawałko, P. Bała, Can zinc alloys be strengthened by grain refinement? A critical evaluation of the processing of low-alloyed binary zinc alloys using ECAP, Mater. Sci. Eng. A. 748 (2019) 357–366, https://doi.org/10.1016/j.msea.2019.01.117.
[36] ASTM E8/E8M-13a, Standard Test Methods for Tension Testing of Metallic Materials, Annu. B. ASTM Stand., 2013, https://doi.org/10.1520/E0008.
[37] W.C. Oliver, G.M. Pharr, An Improved Technique for Determining Hardness and Elastic Modulus Using Load and Displacement Sensing Indentation Experiments, 1992, p. 7.
[38] L. Qian, H. Zhao, Nanoindentation of soft biological materials, Micromachines 9 (2018), https://doi.org/10.3390/mi9120654.
[39] A.K. Gartzke, S. Julmi, C. Klose, S. Besdo, A.C. Waselau, A. Meyer-Lindenberg, H. J. Maier, P. Wriggers, Investigation of degraded bone substitutes made of magnesium alloy using scanning electron microscope and nanoindentation, J. Mech. Behav. Biomed. Mater. 109 (2020) 103825, https://doi.org/10.1016/j.jmbbm.2020.103825.
[40] ASTM G5-14, Standard reference test method for making potentiodynamic anodic polarization measurements, Annu. Book ASTM Stand. (2014), https://doi.org/10.1520/G0005-14.2.
[41] ASTM G31-72, Standard Practice for Laboratory Immersion Corrosion Testing of Metals, Annu. B. ASTM Stand., 2004, https://doi.org/10.1520/G0031-72R04.2, 2004.
[42] ASTM G102-89, Standard Practice for Calculation of Corrosion Rates and Related Information from Electrochemical Measurements, Annu. B. ASTM Stand., 2015, p. 1, https://doi.org/10.1520/G0102-89R15E01.2, 2015.
[43] ISO 8407, Corrosion of metals and alloys — removal of corrosion products from corrosion test specimens, Int. Organ. Stand. (2009), 2009.
[44] C.L.S.I. M07-A9, Methods for Dilution Antimicrobial Susceptibility Tests for Bacteria that Grow Aerobically, Clin, Lab. Stand. Inst., 2012, 2012.
[45] ISO 10993-5, Biological evaluation of medical devices — Part 5: tests for in vitro cytotoxicity, Int. Organ. Stand. (2009), 2009.
[46] ISO 10993-12: 2012(E). Biological evaluation of medical devices–Part 12: sample preparation and reference materials, Int. Organ. Stand. (2012).
[47] S. Liu, D. Kent, H. Zhan, N. Doan, M. Dargusch, G. Wang, Dynamic recrystallization of pure zinc during high strain-rate compression at ambient temperature, Mater. Sci. Eng. A. 784 (2020), 139325, https://doi.org/10.1016/j.msea.2020.139325.
[48] F. Ursini, M. Maiorino, H.J. Forman, Redox homeostasis: the Golden Mean of healthy living, Redox Biol 8 (2016) 205–215, https://doi.org/10.1016/j.redox.2016.01.010.
[49] W. Hussain, A. Mumtaz, F. Yasmeen, S.Q. Khan, T. Butt, Reference range of zinc in adult population (20-29 years) of Lahore, Pakistan, Pakistan J. Med. Sci. 30 (2014) 545–548, https://doi.org/10.12669/pjms.303.4027.
[50] J. Arnaud, M. Touvier, P. Galan, M. Andriollo-Sanchez, D. Ruffieux, A.M. Roussel, S. Hercberg, A. Favier, Determinants of serum zinc concentrations in a population of French middle-age subjects (SU.VI.MAX cohort), Eur. J. Clin. Nutr. 64 (2010) 1057–1064, https://doi.org/10.1038/ejcn.2010.118.
[51] K. Törne, M. Larsson, A. Norlin, J. Weissenrieder, Degradation of zinc in saline solutions, plasma, and whole blood, J. Biomed. Mater. Res. B Appl. Biomater. 104 (2016) 1141–1151, https://doi.org/10.1002/jbm.b.33458.
[52] P. Li, W. Zhang, J. Dai, A.B. Xepapadeas, E. Schweizer, D. Alexander, L. Scheideler, C. Zhou, H. Zhang, G. Wan, J. Geis-Gerstorfer, Investigation of zinc-copper alloys as potential materials for craniomaxillofacial osteosynthesis implants, Mater. Sci. Eng. C 103 (2019), 109826, https://doi.org/10.1016/j.msec.2019.109826.
[53] M.M. Alves, T. Prošek, C.F. Santos, M.F. Montemor, Evolution of the: in vitro degradation of Zn-Mg alloys under simulated physiological conditions, RSC Adv. 7 (2017) 28224–28233, https://doi.org/10.1039/c6ra28542b.
[54] M.B. Kannan, C. Moore, S. Saptarshi, S. Somasundaram, M. Rahuma, A.L. Lopata, Biocompatibility and biodegradation studies of a commercial zinc alloy for temporary mini-implant applications, Sci. Rep. 7 (2017) 1–11, https://doi.org/10.1038/s41598-017-15873-w.
[55] A. Marmur, Measures of wettability of solid surfaces, Eur. Phys. J. Spec. Top. 197 (2011) 193–198, https://doi.org/10.1140/epjst/e2011-01457-4.
[56] F. Witte, K. Yang, J. Wang, D. Zhao, W. Li, Y. Li, T. Xi, J. Meng, L. Qin, Y. Zheng, K. Chan, Y. Yang, Recommendation for modifying current cytotoxicity testing standards for biodegradable magnesium-based materials, Acta Biomater. 21 (2015) 237–249, https://doi.org/10.1016/j.actbio.2015.04.011.
[57] H. Yang, F. Zhang, J. Qian, J. Chen, J. Ge, Restenosis in Magmaris stents due to significant collapse, JACC Cardiovasc. Interv. 11 (2018) e77–e78, https://doi.org/10.1016/j.jcin.2018.02.040.
[58] K. Yamaji, Y. Ueki, G. Souteyrand, J. Daemen, J. Wiebe, H. Nef, T. Adriaenssens, J. P. Loh, B. Lattuca, J.J. Wykrzykowska, J. Gomez-Lara, L. Timmers, P. Motreff, P. Hoppmann, M. Abdel-Wahab, R.A. Byrne, F. Meincke, N. Boeder, B. Honton, C. J. O'Sullivan, A. Ielasi, N. Delarche, G. Christ, J.K.T. Lee, M. Lee, N. Amabile, A. Karagiannis, S. Windecker, L. Räber, Mechanisms of very late bioresorbable scaffold thrombosis: the INVEST registry, J. Am. Coll. Cardiol. 70 (2017) 2330–2344, https://doi.org/10.1016/j.jacc.2017.09.014.
[59] J. Wang, Y. Zhou, Z. Yang, S. Zhu, L. Wang, S. Guan, Processing and properties of magnesium alloy micro-tubes for biodegradable vascular stents, Mater. Sci. Eng. C 90 (2018) 504–513, https://doi.org/10.1016/j.msec.2018.05.005.
[60] Y. Yang, Y. Cheng, S. Peng, L. Xu, C. He, F. Qi, M. Zhao, C. Shuai, Microstructure evolution and texture tailoring of reduced graphene oxide reinforced Zn scaffold, Bioact. Mater. 6 (2021) 1230–1241, https://doi.org/10.1016/j.bioactmat.2020.10.017.
[61] H. Jin, S. Zhao, R. Guillory, P.K. Bowen, Z. Yin, A. Griebel, J. Schaffer, E.J. Earley, J. Goldman, J.W. Drelich, Novel high-strength, low-alloys Zn-Mg (< 0.1 wt% Mg) and their arterial biodegradation, Mater. Sci. Eng. C 84 (2018) 67–79, https://doi.org/10.1016/j.msec.2017.11.021.
[62] E. Mostaed, M. Sikora-Jasinska, J.W. Drelich, M. Vedani, Zinc-based alloys for degradable vascular stent applications, Acta Biomater. 71 (2018) 1–23, https://doi.org/10.1016/j.actbio.2018.03.005.
[63] B. Li, A. Dong, G. Zhu, S. Chu, H. Qian, C. Hu, B. Sun, J. Wang, Investigation of the corrosion behaviors of continuously hot-dip galvanizing Zn-Mg coating, Surf. Coating. Technol. 206 (2012) 3989–3999, https://doi.org/10.1016/j.surfcoat.2012.03.079.
[64] T. Prosek, A. Nazarov, U. Bexell, D. Thierry, J. Serak, Corrosion mechanism of model zinc-magnesium alloys in atmospheric conditions, Corrosion Sci. 50 (2008) 2216–2231, https://doi.org/10.1016/j.corsci.2008.06.008.

[65] C. Yao, Z. Wang, S.L. Tay, T. Zhu, W. Gao, Effects of Mg on microstructure and corrosion properties of Zn-Mg alloy, J. Alloys Compd. 602 (2014) 101–107, https://doi.org/10.1016/j.jallcom.2014.03.025.
[66] J. Niu, Z. Tang, H. Huang, J. Pei, H. Zhang, G. Yuan, W. Ding, Research on a Zn-Cu alloy as a biodegradable material for potential vascular stents application, Mater. Sci. Eng. C 69 (2016) 407–413, https://doi.org/10.1016/j.msec.2016.06.082.
[67] Z. Tang, J. Niu, H. Huang, H. Zhang, J. Pei, J. Ou, G. Yuan, Potential biodegradable Zn-Cu binary alloys developed for cardiovascular implant applications, J. Mech. Behav. Biomed. Mater. 72 (2017) 182–191, https://doi.org/10.1016/j.jmbbm.2017.05.013.
[68] E. Mostaed, M.S. Ardakani, M. Sikora-Jasinska, J.W. Drelich, Precipitation induced room temperature superplasticity in Zn-Cu alloys, Mater. Lett. 244 (2019) 203–206, https://doi.org/10.1016/j.matlet.2019.02.084.
[69] W. Bednarczyk, J. Kawałko, M. Wątroba, P. Bała, Achieving room temperature superplasticity in the Zn-0.5Cu alloy processed via equal channel angular pressing, Mater. Sci. Eng. A. 723 (2018) 126–133, https://doi.org/10.1016/j.msea.2018.03.052.
[70] N.V. Margaritelis, V. Paschalis, A.A. Theodorou, A. Kyparos, M.G. Nikolaidis, Redox basis of exercise physiology, Redox Biol 35 (2020) 101499, https://doi.org/10.1016/j.redox.2020.101499.
[71] C.H. Foyer, G. Noctor, Redox homeostasis and antioxidant signaling: a metabolic interface between stress perception and physiological responses, Plant Cell 17 (2005) 1866–1875, https://doi.org/10.1105/tpc.105.033589.
[72] F. Bonomini, S. Tengattini, A. Fabiano, R. Rezzani, Atherosclerosis and oxidative stress, Japanese, J. Geriatr. 45 (2008) 287–290, https://doi.org/10.3143/geriatrics.45.287.
[73] S. Rahimipour, E. Salahinejad, E. Sharifi, H. Nosrati, L. Tayebi, Structure, wettability, corrosion and biocompatibility of nitinol treated by alkaline hydrothermal and hydrophobic functionalization for cardiovascular applications, Appl. Surf. Sci. 506 (2020), 144657, https://doi.org/10.1016/j.apsusc.2019.144657.
[74] J. Vishnu, M. Calin, S. Pilz, A. Gebert, B. Kaczmarek, M. Michalska-Sionkowska, V. Hoffmann, G. Manivasagam, Superhydrophilic nanostructured surfaces of beta Ti[sbnd]29Nb alloy for cardiovascular stent applications, Surf. Coating. Technol. 396 (2020), https://doi.org/10.1016/j.surfcoat.2020.125965.
[75] A. Reyes-Jara, N. Cordero, J. Aguirre, M. Troncoso, G. Figueroa, Antibacterial effect of copper on microorganisms isolated from bovine mastitis, Front. Microbiol. 7 (2016) 1–10, https://doi.org/10.3389/fmicb.2016.00626.
[76] C.H. Hu, Z.R. Xu, M.S. Xia, Antibacterial effect of Cu2+-exchanged montmorillonite on Aeromonas hydrophila and discussion on its mechanism, Vet. Microbiol. 109 (2005) 83–88, https://doi.org/10.1016/j.vetmic.2005.04.021.
[77] A. Chester, R. Srivastava, G. Awasthi, J. Prakash, A review on bioremediation of heavy metals in contaminated water, IOSR J. Environ. Sci. Toxicol. Food Technol. 8 (2014) 44–50, https://doi.org/10.9790/2402-08714450.
[78] M. Bertuola, A. Miñán, C.A. Grillo, M.C. Cortizo, M.A. Fernández Lorenzo de Mele, Corrosion protection of AZ31 alloy and constrained bacterial adhesion mediated by a polymeric coating obtained from a phytocompound, Colloids Surf. B Biointerfaces 172 (2018) 187–196, https://doi.org/10.1016/j.colsurfb.2018.08.025.
[79] P. Li, C. Schille, E. Schweizer, E. Kimmerle-Müller, F. Rupp, A. Heiss, C. Legner, U. E. Klotz, J. Geis-Gerstorfer, L. Scheideler, Selection of extraction medium influences cytotoxicity of zinc and its alloys, Acta Biomater. 98 (2019) 235–245, https://doi.org/10.1016/j.actbio.2019.03.013.
[80] P.K. Bowen, E.R. Shearier, S. Zhao, R.J. Guillory, F. Zhao, J. Goldman, J. W. Drelich, Biodegradable metals for cardiovascular stents: from clinical concerns to recent Zn-alloys, Adv. Healthc. Mater. 5 (2016) 1121–1140, https://doi.org/10.1002/adhm.201501019.
[81] J. Wang, F. Witte, T. Xi, Y. Zheng, K. Yang, Y. Yang, D. Zhao, J. Meng, Y. Li, W. Li, K. Chan, L. Qin, Recommendation for modifying current cytotoxicity testing standards for biodegradable magnesium-based materials, Acta Biomater. 21 (2015) 237–249, https://doi.org/10.1016/j.actbio.2015.04.011.